(12) INTERNATIONAL APPLICATION PUBLISHED UNDER THE PATENT COOPERATION TREATY (PCT)

(19) World Intellectual Property Organization
International Bureau

(43) International Publication Date
18 January 2024 (18.01.2024)

WIPO | PCT

(10) International Publication Number
WO 2024/015656 A1

(51) International Patent Classification:
A61L 27/52 (2006.01) *A61L 27/54* (2006.01)

(21) International Application Number:
PCT/US2023/067267

(22) International Filing Date:
19 May 2023 (19.05.2023)

(25) Filing Language: English

(26) Publication Language: English

(30) Priority Data:
63/388,245 11 July 2022 (11.07.2022) US

(71) Applicant: **THE REGENTS OF THE UNIVERSITY OF CALIFORNIA** [US/US]; 1111 Franklin Street, 12th Floor, Oakland, California 94607 (US).

(72) Inventors: **MORLEY, Cameron Drew**; 2150 Shattuck Ave., Suite 510, Berkeley, California 94704 (US). **KUMAR, Sanjay**; 2150 Shattuck Ave., Suite 510, Berkeley, California 94704 (US). **CARVALHO, Emily Michele**; 2150 Shattuck Ave., Suite 510, Berkeley, California 94704 (US).

(74) Agent: **OSMAN, Richard**; 530 Lawrence Expy #332, Sunnyvale, California 94085 (US).

(81) Designated States *(unless otherwise indicated, for every kind of national protection available)*: AE, AG, AL, AM, AO, AT, AU, AZ, BA, BB, BG, BH, BN, BR, BW, BY, BZ, CA, CH, CL, CN, CO, CR, CU, CV, CZ, DE, DJ, DK, DM, DO, DZ, EC, EE, EG, ES, FI, GB, GD, GE, GH, GM, GT, HN, HR, HU, ID, IL, IN, IQ, IR, IS, IT, JM, JO, JP, KE, KG, KH, KN, KP, KR, KW, KZ, LA, LC, LK, LR, LS, LU, LY, MA, MD, MG, MK, MN, MU, MW, MX, MY, MZ, NA, NG, NI, NO, NZ, OM, PA, PE, PG, PH, PL, PT, QA, RO, RS, RU, RW, SA, SC, SD, SE, SG, SK, SL, ST, SV, SY, TH, TJ, TM, TN, TR, TT, TZ, UA, UG, US, UZ, VC, VN, WS, ZA, ZM, ZW.

(84) Designated States *(unless otherwise indicated, for every kind of regional protection available)*: ARIPO (BW, CV, GH, GM, KE, LR, LS, MW, MZ, NA, RW, SC, SD, SL, ST, SZ, TZ, UG, ZM, ZW), Eurasian (AM, AZ, BY, KG, KZ, RU, TJ, TM), European (AL, AT, BE, BG, CH, CY, CZ, DE, DK, EE, ES, FI, FR, GB, GR, HR, HU, IE, IS, IT, LT, LU, LV, MC, ME, MK, MT, NL, NO, PL, PT, RO, RS, SE, SI, SK, SM, TR), OAPI (BF, BJ, CF, CG, CI, CM, GA, GN, GQ, GW, KM, ML, MR, NE, SN, TD, TG).

Published:
— *with international search report (Art. 21(3))*
— *before the expiration of the time limit for amending the claims and to be republished in the event of receipt of amendments (Rule 48.2(h))*

WO 2024/015656 A1

(54) Title: CELL-MICROGEL ENCAPSULATION IN INJECTABLE FORMULATIONS

(57) Abstract: Systems, devices, compositions and methods configured for delivering microgel-encapsulated cells in injectable formulations, comprising cells embedded within pore space of microscopic hydrogel particles, wherein while ensconced in this packed bed of microgels, the cells are protected from the shear stresses and shear stress gradients.

Cell-microgel Encapsulation in Injectable Formulations

[001] Introduction

[002] Administration of cell-based therapeutics has shown increasing promise for disease treatment and regenerative medicine. When the anatomical target is diffuse, such as in the case of bone marrow transplantation, cells may be delivered intravenously, leveraging diffusion and convection through the vasculature for distribution throughout the body. However, highly localized delivery of cells to solid tissues such as the brain has proven much more challenging because the formulation must be sufficiently liquid-like to permit injection but sufficiently solid-like to remain at the target site. Encapsulation of cells in 3D hydrogels prior to injection into tissue is emerging as an attractive strategy to address the latter challenge[1-5]. Once delivered, hydrogels can provide a mechanically stable engraftment niche for engineered cells and thus improve cell survival and function[3,6]. However, the covalent crosslinking strategies often used to form these hydrogels can compromise injectability and potentially subject cells to mechanical trauma as the hydrogel can be damaged during injection[7,8]. Thus, there is a recognized need to improve the injectability of hydrogel-based formulations. Progress has been made by developing hydrogels with temporally tunable crosslinking kinetics, such as those employing click-chemistries[9,10], and shear-thinning properties to facilitate flow during injection and control over solidification upon delivery. Despite promising cell survival *in vitro*, viability and engraftment *in vivo* can often fall below 5%[3,6], where it has been hypothesized that shear thinning hydrogel characterization via rheology poorly translates to flow properties through thin needles[11]. Thus, there is a need for improvement upon shear thinning injectables with clear documentation of the injectables' performance after near-instantaneous shear.

[003] To improve hydrogel injectability, the field has begun to explore hydrogel crosslinking chemistries that can break and re-form bonds to provide shear-protection during injection and solidify once delivered. For example, the dynamic noncovalent crosslinks between guest-host pairs, such as adamantane and cyclodextrin (AC), allow transient rupture and re-formation in response to shear stress[5]. Similarly, others have demonstrated control over the hydrogel fluid-to-solid phase transition, exploiting materials that are self-healing (e.g. gelatin), crosslinked with non-AC dynamic chemistries, such as hydrazones, and responsive to environmental stimuli, such as pH and temperature[12,13]. Electrostatic forces between biopolymers have also been leveraged to tune shear-thinning and self-healing properties[14]. Other approaches encapsulate cells within biodegradable hydrogel shells, entirely avoiding the use of crosslinks to control injectability[15]. All these approaches can provide shear protection in their respective contexts and exhibit incredible promise for regenerative medicine applications. However, injectability and

stability upon delivery often trade off in these systems, such that improving performance in one property generally compromises the other. Further, these formulations are optimized for a given cell-therapy and tissue combination. Independent tuning of material shear-protection and engraftment-facilitation is needed to accommodate new cell therapies or to be more broadly applicable to multiple tissues.

[004] Packed microscale hydrogel particles (microgels), which are widely used in 3D cell culture and biofabrication[16-19], have recently been explored as a strategy for balancing injectability and shear-protection[20-23]. In the jammed state, these materials reconfigure and flow like liquids at high shear rates but also demonstrate solid-like yield stress properties at low shear rates[17]. The micro-porous architecture of microgels facilitates cell encapsulation between particles, which physically shields cells from intra-needle velocity gradients and high shear stresses at no-slip boundaries. Previous studies have shown that particle shape and size influence injectability and engraftment[21,22], and dynamic inter-particle AC crosslinking improves shear-protection and viability for cells encapsulated between spherical, but not irregularly shaped, particles[22].

[005] Summary of the Invention

[006] The invention enables customized shear-protection for cell therapies.

[007] The invention provides an injectable formulation strategy in which spherical hyaluronic acid (HA) microgels are dynamically crosslinked with guest-hose pair (e.g. AC) crosslinks and decorated with RGD-based peptides to enable 3D integrin engagement. Just as the force-sensitivity of AC crosslinks has been exploited to fabricate stress-relaxing bulk hydrogels, we find that reversible AC crosslinks between microgel particles support the shear-thinning behavior needed for injectability while stabilizing the microgel pack post-injection with minimal residual stress. We 3D print mixtures of cells and microgels with varying AC densities into continuous, AC-free HA microgels to demonstrate their shear-protecting efficacy.

[008] The invention provides methods and compositions in which cells are ensconced in the pores between microscopic granular hyaluronic acid (HA) hydrogels (microgels), which may themselves be reversibly crosslinked through guest-host pair (e.g. adamantane-cyclodextrin (AC)) interactions.

[009] The invention provides systems, devices, compositions and methods configured for delivering microgel-encapsulated cells in injectable formulations, essentially as disclosed herein.

[010] In aspects and embodiments the invention provides:

[011] An injectable formulation system comprising cells embedded within pore space of microscopic hydrogel particles, wherein while ensconced in this packed bed of microgels, the

cells are protected from the shear stresses and shear stress gradients, wherein the chemical composition of the particles can be engineered to promote longevity and generation of the appropriate cellular phenotypes, and wherein the system is optionally configured to provide temporal control over exposure to growth factors, cytokines, and pharmacologic agents.

[012] An injectable formulation system as disclosed and configured to effect swapping the solvent surrounding the cell laden hydrogel therapy and subsequently protecting the embedded cells during delivery to facilitate functional integration post-transplantation.

[013] A microgel-based delivery system substantially as described herein and configured to encapsulate cells to protect the cells from physical damage due to shear and extensional flows during the transplantation process.

[014] A microgel-based delivery system substantially as described herein and configured to be mechanically tunable, e.g. to increase the rate of cell engraftment post-transplantation by providing scaffolding for cells to migrate and integrate into the host circuitry.

[015] A microgel-based delivery system substantially as described herein and configured for practical application to cell transplantation.

[016] A microgel-based delivery system substantially as described herein and configured to provide a stable three-dimensional niche at the delivery site.

[017] A microgel-based delivery system substantially as described herein and configured to encapsulate cells in the pore space between microscopic hydrogel particles (microgels), and employing yield stress fluid properties of packs of microgels to protect the cells from mechanical stress during delivery and to facilitate integration to the native tissue, wherein during delivery, the packs of microgels undergo plug flow in which the pressure drop across the length of the pipe is compensated (preferably solely) by frictional forces at the interface between the pipe wall and microgels, and wherein at the delivery site, the pack of microgels behave as an elastic solid across the range of physiological frequencies and provide a stable 3D culture paradigm to support engraftment.

[018] A microgel-based delivery system substantially as described herein and configured to encapsulate cells in the pore space of the microgel, and confine the formulation to a fixed volume to facilitate perfusing liquid freeze/thaw or maintenance media, differentiation factors, and anti-inflammatory agents prior to delivery to the tissue, making the formulation ammenable to transport and storage.

[019] A microgel-based delivery system substantially as described herein and configured for use as a vehicle for delivery of therapeutic cells into an animal host, preferably wherein it can be used to encapsulate and deliver differentiated human pluripotent stem cells in regenerative medicine applications, or used to deliver differentiated neural cell types for regenerative

therapies targeting a central nervous system pathology.

[020] A method of delivering microgel-encapsulated cells in injectable formulations essentially as described herein, the method comprising:

[021] employing yield stress fluid properties of packs of microgels to protect the cells from mechanical stress during delivery and to facilitate integration to the native tissue,

[022] wherein during delivery, the packs of microgels undergo plug flow in which the pressure drop across the length of the pipe is compensated solely by frictional forces at the interface between the pipe wall and microgels,

[023] wherein at the delivery site, the pack of microgels behave as an elastic solid across the range of physiological frequencies and provide a stable 3D culture paradigm to support engraftment.

[024] A method of delivering microgel-encapsulated cells in injectable formulations essentially as described herein, the method comprising embedding cells within the pore space of microscopic hydrogel particles, wherein while ensconced in this packed bed of microgels, the cells are protected from shear stresses and shear stress gradients.

[025] A method of delivering microgel-encapsulated cells in injectable formulations essentially as described herein, the method comprising steps:

[026] a) mix aqueous and organic phases to perform inverse emulsion Michael addition crosslinking of HA w/DTT to generate spherical hydrogels; b) homogenize mixture with fine blades to generate droplets whose diameters closely match those of cells. Smaller droplets are required for delivery through a thin needle / cannula; c) wash microgels of organic phase to rid of excess organic phase (e.g. kerosene) and surfactant; d) swell microgels in desired growth media to provide nutrient reserve for cells; e) pipette mix cells into microgels at a volume fraction <20% to ensure shear protection capabilities of microgels is not diluted by cells; g) load mixture into custom syringe (see diagram) to provide storage and transport, and facilitate cryopreservation; and h) inject into patient to provide cell therapy.

[027] A system, device, composition or method herein, wherein the adamantane and cyclodextrin (AC) concentration is less than a critical AC concentration wherein the stress required to break AC bonds and drive flow during injection exceeds microgel yield stress.

[028] A system, device, composition or method herein, comprising use of highly monodisperse spherical microgels.

[029] A system, device, composition or method herein, comprising a microgel fabrication protocol to generate particle diameters on the same order of magnitude as cell diameters, ensuring that the largest objects are 10x smaller than the roughly 200 μm (27 – 30G) cannula diameter commonly used in delivery of cell therapies..

[030] A microfluidic platform configured to formulate NSC droplets within packs of HA microgels (Fig. 20), wherein cells are matured in spheroids using agar wells, low adhesion dishes, or hanging drop methods and subsequently isolated and encapsulated in the microgels prior to transplantation.

[031] An injectable formulation deliver device providing solvent exchange, configured to confine the injectable formulation to a fixed volume with porous filters on the inlet and exit (Fig. 21), wherein microgels and cells are contained within this volume due to being larger than the mesh of the filters, such that different solvents can be flushed through the pores of the formulation.

[032] The invention encompasses all combinations of the particular embodiments recited herein, as if each combination had been laboriously recited.

[033] Brief Description of the Drawings

[034] Fig. 1a-c. Microgel-based injectable assembly and testing platform. (a) Inverse emulsion polymerization process of MeHA and DTT. Residual methacrylate groups are used to functionalize AC and cell adhesion peptide, RGD. Cells are encapsulated between these microgel particles to (b) facilitate shear protection and provide a stable 3D engraftment niche post-injection. (c) 3D printing platform to identify the efficacy of shear protection. This platform also facilitates injection into hydrogels to mimic tissue injection *in vivo*.

[035] Fig. 2a-b. Quantifying 3D NSC attachment. (a) Cell seeding density and timelapse (top) and colorimetric depth visualization (bottom) of protrusions and networks. Images shown are maximum intensity projections of the (top) fluorescent data and (bottom) grayscale height map. (b) Quantification of maximum protrusion depth as a function of seeding density, ϕ_0, and time, t. Bars represent the mean maximum protrusion depth (n = 3-5).

[036] Fig. 3a-c. Retaining injected cellular cargo. (a) Injection into hydrogels to measure volume retention capacity of granular materials. (b) NSC-laden liquid (left) and NSC-laden microgel (right) injectable. Images shown are maximum intensity projections of confocal z-stacks. White dotted circle represents the 30G needle diameter. Scale bar = 250 mm. (c) Quantification of relative retention volume, V_r.

[037] Fig. 4a-b. 3D printing injectable formulations into bare HA microgels. (a) Live (green) and dead (red) cells after 24 h in culture post-injection into our 3D printing sacrificial microgel material. Scale bar = 100 um. Quantification of viability for cells injected (b) at controlled shear rates on the 3D printer and hand injected. Dashed line corresponds to the 70% viability target.

[038] Fig. 5a-d. Rheological characterization of HA-AC microgels. (a) Oscillatory rheology shows $G'>G''$ and frequency independence of G' for all AC concentrations. (b) Unidirectional

rheology reveals Herschel-Bulkley (HB) behavior for low, shear thinning fluid behavior for high AC concentrations. Data is normalized by $\langle G'(\omega)\rangle_\omega$, from the oscillatory sweep and error bars represent the minimum and maximum σ across the three batches for a given $\dot{\gamma}$. (c) Peak relaxation modulus normalized by $\langle G'(\omega)\rangle_\omega$ shows lower stress magnitudes are required to initiate flow in the low AC microgels. (d) Stress relaxation normalized by peak relaxation modulus shows increased stress relaxation capabilities of AC microgels.

[039] Fig. 6a-f. AFM on HA-AC hydrogels. (a) Sample preparation for AFM measurements. (b) Representative indentation and retraction curve including calculated metrics for quantifying adhesion. (c) Representative indentation curves fit using the approximation of Hertzian conical contact. (d) Young's modulus values from curves acquired on samples with a bare probe. (e) Adhesive work and (f) adhesive stress calculation for AC samples indented with an adamantane functionalized probe. Box plots shown have maxima and minima corresponding to the 1 and 99 percentiles respectively (n=100).

[040] Fig. 7a-b. HA microgel size characterization. (a) Residual methacrylate binding sites for AC and RGD using a cysteine labeled FITC tag. (b) Size distributions show we can produce cell sized particles.

[041] Fig. 8a-b. MeHA and HA microgel characterization for 3D printing preparations. (a) MeHA Viscometry shows a slight shear thinning behavior at low shear rate and Newtonian fluid-like behavior at high shear rates. (b) We observe a dependence of the 2% HA, 0.7 molar ratio DTT microgels' elastic modulus on centrifugal force. The dotted line represents the bulk hydrogel elastic modulus.

[042] Fig. 9. After 72 h in culture, NSCs form spheroids and extend protrusions to interact with 3D microenvironment. Images shown are maximum intensity projections of a 5 um z-stack. The center of the spheroid is intentionally saturated to allow visualization of the protrusions.

[043] Fig. 10. NSC dispersal in liquid media with RGD. Scale bar = 250 um.

[044] Fig. 11a-c. 3D printing resolution and feature size prediction. (a) Mixing 1 um fluorescent TRITC particles with MeHA, we demonstrate the ability to predictably generate features of various sizes. (b) Mixing NSCs with MeHA, we find feature size to be constant across many tested Q and v. (c) We demonstrate that multiple injectables and support baths facilitate predictable printed features. However, NSCs sediment in MeHA during printing, generates fragmented features whose diameter is dictated by the 30G needle diameter.

[045] Fig. 12. Viability time-lapse quantification of MeHA control at shear rates of 250, 1250, and 4125 s^{-1}.

[046] Fig. 13a-c. NSC longevity when stored in cryovials. (a) Cells dispersed in liquid media will settle to the bottom of the container while cells dispersed in microgels are supported in 3D

during culture. (b) NSCs dispersed in liquid media and (c) microgels, probed for viability over time.

[047] Fig. 14a-c. Confirming aberrant AC microgel rheology is not a function of sample preparation. (a) Unidirectional rheology for three microgel fabrications using two different MeHA stocks. (b) Representative unidirectional rheological curves for the medium and high AC concentrations. (c) Oscillatory rheology comparison from the same samples shown in (a).

[048] Fig. 15a-b. Poisson's Ratio measurements on HA hydrogels. (a) The 25 mm diameter rheometer probe compresses an 8 mm diameter x 1 mm thick HA hydrogel sample. (b) Deformations are applied stepwise, where we calculate Poisson's Ratio for each deformation. The dotted line corresponds to the cumulative mean Poisson's Ratio.

[049] Fig. 16a-c. AFM controls and representative curves. (a) Comparison of approach curves from indenting AC hydrogels with a bare probe. (b) Comparison of approach curves from indenting AC hydrogels with an adamantane-functionalized probe. (c) Retraction curves for bare and high AC concentration hydrogels.

[050] Fig. 17a-f. Effect of residual surfactant on microgel particles. (a) PBS only washed microgels display inter-particle aggregation. (b) Quantification of microgel size for both wash conditions. (c) Reduced shear protection at high shear rate. (d) PBS only washed samples display decreased G' for all frequencies and (e) σ for all shear rates. (f) Reduced attachment in PBS only washed microgels with 0.2 $mgmL^{-1}$ RGD. Scale bars for (a) and (b) are 10 um.

[051] Fig. 18. Comparison of two methods of calculating viability.

[052] Fig. 19. Image processing steps for 3D hydrogel injections. Scale bar = 250 um.

[053] Fig. 20. Method of encapsulating NSC spheroids in microgels; enlargement depicts cell spheroid in HA microgel

[054] Fig. 21. Schematic of injectable formulation delivery device; filters are option based on loading/flushing.

[055] Description of Particular Embodiments of the Invention

[056] Unless contraindicated or noted otherwise, in these descriptions and throughout this specification, the terms "a" and "an" mean one or more, the term "or" means and/or. It is understood that the examples and embodiments described herein are for illustrative purposes only and that various modifications or changes in light thereof will be suggested to persons skilled in the art and are to be included within the spirit and purview of this application and scope of the appended claims. All publications, patents, and patent applications cited herein, including citations therein, are hereby incorporated by reference in their entirety for all purposes.

[057] The invention provides novel injectable formulations in which we embed cells within the pore space of microscopic hydrogel particles. While ensconced in this packed bed of microgels, the cells are protected from the shear stresses and shear stress gradients that other injectable formulations would fall subject to. In addition, the chemical composition of these particles can be engineered to promote longevity and generation of the appropriate cellular phenotypes. Furthermore, the system supports temporal control over exposure to growth factors, cytokines, and pharmacologic agents.

[058] The invention provides a method of swapping the solvent surrounding the cell laden hydrogel therapy and subsequently protecting the embedded cells during delivery to facilitate functional integration post-transplantation.

[059] The microgels described here encapsulate cells to protect the cells from physical damage due to shear and extensional flows during the transplantation process. Further, the microgels may be mechanically tuned to increase the rate of cell engraftment post-transplantation by providing scaffolding for cells to migrate and integrate into the host circuitry.

[060] The formulations may be configured for cell-transplantation pre-packaged at a cGMP facility, frozen, shipped, and thawed just prior to delivery to the patient. Furthermore mixtures of microgels and cells can be cultured *in vitro* to mature for extended periods of time prior to implantation.

[061] Features and advantages of the invention include:

[062] Plug flow at high shear rate: Generating plug flow in injectable formulations has been documented to improve cell viability. Traditionally, plug flow (i.e. constant velocity profile across the cross-section of the needle) is achieved by using shear thinning hydrogels to generate layer of lubrication between the cells and needle wall[14, 15]. Instead, we impose plug flow by creating slip between the microgel-needle interface. While both approaches produce plug flow, our approach features solid-like behavior during flow at higher shear rates, allowing us to deliver the injectable formulations to tissue orders of magnitude more rapidly. Further, this approach allows for a wider range of hydrogel crosslinking chemistries (e.g. covalent crosslinking), because of the complete decoupling of intra- and inter-microgel assembly mechanisms. This is achieved by functionalizing the HA backbone with guest-host molecules adamantane and cyclodextrin.

[063] Modularity: Many injectable formulations are highly tailored to a specific application. For example, engraftment of dopaminergic neurons has been shown to be facilitated by hyaluronic acid (HA), a major extracellular matrix (ECM) polysaccharide found within brain parenchyma[16]. Our approach permits fabrication of HA microgels that feature all the benefits of injectable HA-hydrogels without subjecting them to high shear stresses arising from viscous pre-

polymerized solutions or shear thinning hydrogels. In embodiments the invention further provides improved engraftment by embedding stromal cells (glia, endothelial cells, etc.) together with secondary ECM components in the inter-microgel pore space. Using this approach, the invention provides formulations whose materials and chemistries can be tailored to best fit the cell type and application.

[064] Perfusability: Our approach also greatly eases co-delivery of biologics (e.g. growth factors) and small molecules. For example, T cells delivered during Adoptive Cell Transfer (ACT) are treated with IL-2 to trigger metabolic and transcriptional events such as differentiation and proliferation[18]. By embedding these cells in a hydrogel, the IL-2 treatment step occurs in 2D *in vitro* prior to assembling the injectable formulation[18]. In a cell laden microgel-based system, the IL-2 treatment can be applied to the formulation itself due to its porous macrostructure. Similarly, we can perfuse media formulations tailored for stem cell differentiation or freeze and thaw cycles (e.g. supplemented with DMSO), which eliminates many logistical constraints surrounding transportation of current injectable formulations.

[065] Related materials are being used in bulk hydrogel injectable formulations,[15, 19, 20] however our approach offers distinct advantages in performance characteristics (herein), and no existing cell delivery technology similalry supports the logistical and practical requirements of producing, transporting, and delivering the formulation to the patient from benchtop-to-bedside.

[066] The microgel-based injectable systems disclosed here can support any ECM and/or delivered cell; in particular embodiments it is configured to be a vehicle for NSC-derived neurons for therapeutic engraftment. To briefly review an exemplary embodiment of our methodology, we mix NSCs into the pore space between microscopic hydrogel particles. We use an inverse emulsion to fabricate the hydrogels, enabling us to ensure that they remain spherical. This approach can be used to fabricate microgels of many different compositions, and in particular, formulations configured for injection with NSCs from HA. These HA microgels can be functionalized with peptides containing the RGD motif, modified with guest-host molecules to tune the mechanical properties of the system, and secondarily crosslinked to form bulk hydrogels.

[067] The microgels can be chemically and mechanically tuned to increase the range of shear rates at which the formulation undergoes plug-like flow and protects the NSCs from shear stress. In one example, we demonstrate the ability to functionalize the HA microgels with Adamantane and Cyclodextrin to obtain guest-host crosslinking between multiple microgel particles. In another method, we demonstrate the ability to systematically tune the degree of functionalization of the HA microgels and measure the resulting changes in mechanical properties. With increasing degree of functionalization, we observe changes in the rheological characterization

consistent with maintaining solid-like behavior during forced flow. The underlying chemistries have been used in other applications[21], ours is the first utilizing the guest-host interaction at the surface between two microgels in order to increase the injectable's solid-like behavior.

[068] Another application of the invention is to formulate NSC droplets within packs of HA microgels using a microfluidic platform (Fig. 20). Instead of homogeneously mixing individual cells into the microgel, the cells are matured in spheroids using agar wells, low adhesion dishes, or hanging drop methods and subsequently isolated and encapsulated in the microgels prior to transplantation. This approach is well-suited to the transplantation of neural or immature cells that generally better survive in high cell density structures. For example, neural progenitor transplantation is a potential therapy for neurodegenerative disorders such as Amyotrophic Lateral Sclerosis (ALS)[22]. Our invention enables purification procedures[23] (e.g. sorting cells for expression of specific markers) prior to transplantation.

[069] In order to exchange solvents, our system can be configured to confine the injectable formulation to a fixed volume with porous filters on the inlet and exit. (Fig. 21). While the microgels and cells are contained within this volume due to being larger than the mesh of the filters, we can flush different solvents through the pores of the formulation. Our approach is amenable to perfuse cells in freezing media, prepare them for cryostorage, and transport the resulting formulation to the point of care. There, the formulation can be slowly thawed and perfused with fresh maintenance media without the need for any additional tools than the medium and a syringe.

[070] Intra-microgel adhesivity in granular injectables using a 3D bioprinting platform

[071] Injectable hydrogels are useful for the therapeutic delivery of cells to tissue. These materials can both protect cells from mechanical stress during injection and provide a stable three-dimensional niche at the engraftment site that promotes survival and function. Hydrogels that provide both shear protection and engraftment stability commonly employ methods of reversible crosslinking, such that the material behaves as a viscous fluid during delivery and an elastic solid at the delivery site. Encapsulation within microscopic granular hydrogels (microgels) eliminates shear stress exposure to the cellular cargo, however, liberation of cells at the delivery site using this approach usually requires a biodegradable carrier. While hydrogel-based approaches have shown to reduce shear stress during delivery, rates of stem cell survival and engraftment still often fall below 5%. Here we disclose a hybrid approach, where we ensconce cells, such as neural stem cells (NSCs) in the pores between cell-sized microgels (such as hyaluronic acid). An innovation in our approach is the use of these microgels in sacrificial 3D printing, enabling us to systematically investigate the effect of intra-needle position and intra-microgel adhesivity on cell survival. We functionalize them using guest-host molecules (such as

adamantane and cyclodextrin) to tune intra-microgel adhesivity and with RGD peptide to facilitate cell-matrix interactions post-injection. Our results demonstrate the control over the mechanical properties of our injectable formulation and how these mechanical changes mediate cell viability and matrix attachment. The use of our 3D printing platform enables evaluation of injectable efficiencies, including cell viability with increasing solid-like properties during injection via intra-microgel adhesion as a function of space.

[072] Examples

[073] Microgels as an injectable and as a platform for injectable testing

[074] *HA microgel-based shear protecting formulation*

[075] We developed a shear protecting formulation using HA microgels stabilized by two types of crosslinks: static covalent linkages to set intrinsic microgel mechanical properties, and dynamic AC-based inter-microgel crosslinks that break and reform in response to shear. To introduce chemical handles for both crosslinking and peptide conjugation, we methacrylate-functionalized HA (median MW = 60 kDa) to form HA-methacrylate (MeHA) as described in Methods and our earlier studies[24,25]. We further took advantage of the chemical versatility of thiol-reactive MeHA to conjugate RGD peptides to enhance cell adhesion. We then fabricated spherical microgels by reacting MeHA with a 1,4-Dithiothreitol (DTT) crosslinker in the aqueous phase of an inverse emulsion (**Fig. 1**a, see Methods). To confirm availability of methacrylate groups post-crosslinking for AC and RGD molecules, we added a fluorescently labeled cysteine (FITC-cysteine) to packs of bare HA microgels. Epifluorescence imaging (see Supplementary Information, Fig. 7a) revealed monodisperse microgel populations (n = 100, PDI = 0.01) with a mean diameter of 10.0 um (Fig. 7b). We tuned our microgel fabrication protocol to generate particle diameters on the same order of magnitude as cell diameters, ensuring that the largest objects are 10x smaller than the roughly 200 um (27 – 30G) cannula diameter commonly used in delivery of cell therapies[11]. Subsequent centrifugation ensures that the microgels are in the jammed state and can provide shear protection to cellular cargo by reducing the intra-needle velocity gradient (Fig. 1b). Consistent with past reports[26], we found that centrifugation force strongly influences rheological properties, providing a secondary level of control (Fig. 8b). In our system, increasing centrifugal force increased the storage modulus of the microgel pack, asymptotically approaching the bulk hydrogel limit. We therefore proceeded with microgels centrifuged at 4000 $\times g$ and subsequently conjugated with cysteine-modified AC and RGD, which were then mixed with cells before testing their efficacy at reducing intra-needle shear stress and facilitating 3D engraftment (Fig. 1c).

[076] *Neural stem cell (NSC) engraftment*

[077] In these examples we chose to work with murine neural stem cells (NSCs, see Methods),

which can give rise to neurons in the brain and show great promise as injectable cell sources in neuroregenerative applications[3,27,28] but suffer from low rates of engraftment. Engraftment efficiency in real tissue is calculated as the percentage of viable or attached cells from the initial injected cell count and is the result of a series of potentially traumatic events: cells flow through a narrow needle into a viscoelastic tissue, where the retained and survived fraction must attach and grow within the injected 3D matrix and integrate into the native tissue on longer time scales. We sought to validate our injectable microgel platform by first demonstrating the ability of the granular material to support 3D NSC network formation.

[078] To facilitate NSC network formation, we functionalized the microgels with an RGD-based adhesive peptide (see Methods). We lightly pipette-mixed NSCs with HA-RGD microgels to create homogenous cellular dispersals and cultured them in 3D for up to 5 days. We found that NSCs self-assemble into spheroids that can extend protrusions into the microgel pack after 24 h (Fig. 9). We hypothesized that increasing cell density would enable connection of multiple spheroids via these protrusions to form larger cellular networks, a morphological phenotype that could facilitate engraftment. We varied RGD concentration between 0 – 0.2 $mgmL^{-1}$ and observed multicellular network assembly across all RGD concentrations; however, the z-position of spheroid-connecting protrusions appeared to depend on RGD concentration. NSCs cultured in bare microgels generated protrusions only at the interface of the glass bottom of the well (z = 0 um) (bottom panel, **Fig. 2**a, see Methods). In contrast, network-forming protrusions can be observed hundreds of microns above the glass bottom in higher-RGD concentration microgel packs (Fig. 2a). We quantified the maximum depth of spheroid-connecting protrusions as a function of seeding density and time (Fig. 2b, see Methods) and found that bare and 0.002 $mgmL^{-1}$ RGD microgels did not induce protrusions at large z-depths for most seeding densities and times, indicating that NSCs do not efficiently form 3D connections in these conditions. Instead, only small, discrete spheroids are observed at large z-depths (white circles, Fig. 2a, bottom). In contrast, NSCs in the 0.02 and 0.2 $mgmL^{-1}$ RGD microgels form protrusions and networks at higher z-depths with increasing time for cellular seeding volume fractions, ϕ_0, of 10%. In the higher cell density dispersal, this trend held for 0.02 $mgmL^{-1}$ RGD but not 0.2 $mgmL^{-1}$ RGD, with protrusion depth decreasing with increased ϕ_0. We hypothesize that increased cell density and higher RGD concentration leads to more rapid network formation, decreasing the need for spheroid-connecting protrusions. Nonetheless, we observe successful NSC network formation across many RGD concentrations, seeding densities, and times.

[079] The dependence of spheroid and network formation on seeding density and time is consistent with previous work demonstrating a percolation threshold for cellular dispersals in granular media[16]. In our work, lower cell density corresponds to network forming protrusions at

greater z-depths, and similarly, higher RGD concentration facilitated network formation for both seeding densities. Our goal was not only to showcase the ability of this matrix to support NSC network formation, but also to leverage these data to determine input cell volume fraction for injectable testing. We sought to minimize cell density, which was chosen to be 10 – 15% (see Supplementary Information) and maximize microgel density to preserve the materials' shear protecting capabilities during flow through narrow needles without inhibiting multicellular network formation after injection. We also dispersed NSCs in liquid media with 0.02 – 1.00 $mgmL^{-1}$ unreacted RGD and cultured them on untreated glass-bottom dishes for 24 h to determine if protrusions inherently develop at the glass interface (Fig. 10). The NSCs aggregated like their microgel-encapsulated counterparts but did not display the elongated morphologies that we observed at the microgel-glass bottom interface, suggesting microgels facilitate network formation at interfaces as well.

[080] We next asked whether the microgel injectable retains more of the injected volume of cells than their liquid counterpart, thus improving NSC engraftment potential. To isolate this aspect of the injection pipeline, we slowly performed injections of NSCs mixed with either liquid medium or bare HA microgels into bulk HA hydrogels with our custom 3D bioprinter (**Fig. 3**a, see Methods). The use of precise linear motion stages allows us to delicately enter tissue-like hydrogels and systematically evaluate the volume of cargo retained when injected into viscoelastic solids. After 12 h of 3D culture post-injection , we observed viable cells in both the microgel and liquid media injectables, albeit with distinctly unique injected volumetric morphologies. The deformation imposed by the liquid injectable on the HA hydrogel creates a small cavity, roughly the diameter of our 30G (I.D. = 160 um) needle, with a crack propagating outward (Fig. 3b). This brittle failure event is expected given the rigid nature of the surrounding covalently crosslinked HA[29]. In contrast, the yield stress capability of the microgel injectables reinforced the cracks generated by injection and imposed plastic deformation on the hydrogel, generating a larger oval-shaped cavity (Fig. 3b). We measured a 7.5-fold increase in retention volume for the microgel injectable relative to the liquid medium control (Fig. 3c, see Methods and Supplementary Information).

[081] *3D printing into microgels: determining sources of mechanical trauma in granular injectables*

[082] We next investigated the ability of our microgel-based formulations to support shear protection and cell viability during injection using our 3D bioprinter, benchmarking their performance against their liquid counterparts (Fig. 1c). Testing injectable efficiency using this embedded 3D printing approach holds many key strategic advantages. When coupled with rheological characterization, we can predict shear stress as a function of shear rate by precise

control of flow rate on our 3D printer. Most importantly, embedded printing in microgels (Fig. 1c – *i*) preserves the spatial distribution of cells as they exit the needle, allowing us to identify physical regions of cell-damaging shear stresses. When injecting Newtonian or shear thinning liquids, for example, we would expect shear stress-induced cell death to be highest at the needle wall and gradually decrease toward the center of the needle. If this cargo were being injected into liquid media, the shear history of each cell would be lost, eliminating the ability to directly observe cell death at the no-slip, high shear stress boundary. Access to shear history could be informative in developing injectable formulations, especially for non-Newtonian or granular microgel injectables, where the flow profile is rate-dependent and underlying shear-protection limitations are still poorly understood[11,22].

[083] To first demonstrate that embedded 3D printing preserves the shear history and quantify the shear stress required to damage NSCs, we printed mixtures of NSCs with the microgels' Newtonian liquid precursor, 3% (w/w) uncrosslinked MeHA, into bare (i.e. free of AC and RGD) HA microgels. We chose an MeHA concentration by identifying the viscosity and shear rate required to generate 5 – 100 Pa of shear stress at the needle wall, as previous reports document cell death and membrane rupture between 30 – 150 Pa[30,31] (**Fig. 4**a, see Supplementary information). To increase shear stress, we varied shear rate from 250 – 4125 s^{-1}, and modified printing needle translational velocity proportionally in order to achieve 300 um diameter, thereby minimizing potential negative effects of nutrient depletion at the center of printed NSC features in 3D culture. We confirmed the Newtonian fluid-like behavior of MeHA by showing $\sigma \sim \dot{\gamma}$ across the range of tested shear rates with unidirectional rheology (Fig. 8a). We predict printed feature cross-sectional area, A, similar to our previous reports[17] (see Methods, Fig. 11). In these MeHA prints, we observed increased cell death (red, Fig. 4a, see Methods) with increasing shear rate and localization of dead cells at the outermost layer of the printed object.

[084] To confirm that shear stress is the dominant contributor to cell death, we measured cell viability of printed NSCs and MeHA mixtures into bare HA microgels after 6, 24, and 72 h in 3D culture (see Supplementary Information). We observed minimal decreases in viability at the lowest shear rate and for all shear rates evaluated at 6 h followed by decreased viability at 24 h (Fig. 12). Shear rate-dependent viability trends remained constant between the 24 and 72 h time points. We also gently pipette mixed NSCs into our HA microgels and cultured them for up to 7 days (Fig. 13a-c). These results confirmed that neither the HA microgel support bath nor the MeHA impose acute cytotoxicity and negative effects observed from injection reach a plateau at 24 h, where we probe the effects of mechanical damage during injection (Fig. 12, 13a-c).

[085] We repeated the shear rate sweep with mixtures of bare microgels and NSCs into bare

HA microgels and found increased cell viability relative to their liquid MeHA counterparts. However, cell viability at the highest shear rate still fell below 70%, which is required for FDA approval of injectable cell formulations[32]. In contrast to the MeHA prints, we observed dead cells and increasing co-localization of the live and dead channels distributed throughout the printed feature, suggesting shear stress is instead generated between microgels. We hypothesized that cellular damage could be driven by increased frequency of microgel rearrangement and speed at which microgels slide past one another at high shear rates.

[086] To suppress microgel rearrangements and consequent intra-injectable shear stress, we printed mixtures of NSCs and AC-functionalized HA microgels into bare HA microgels. We functionalized our HA microgels with AC concentrations of 0.01 (low), 0.05 (medium), and 0.11 (high) molecule-to-HA monomer repeat unit molar ratio and repeated the injection shear rate sweep. We found that the low and medium AC densities support higher cell viability than MeHA, bare HA microgels, and high-AC microgels (Fig. 4b). The NSC laden AC microgel mixtures were then hand-injected into bare HA microgels, increasing the shear rate to roughly 20,000 s^{-1}. Strikingly, we found that viability fell with increasing AC concentration, and low AC concentration yielded 70% NSC viability (Fig. 4c).

[087] *Determining the mechanism for decreased cell viability in high AC concentration microgels*

[088] We next sought to understand the mechanism behind decreased cell viability in the high AC concentration microgels. Cell viability in our microgel injectable formulations appears to be independent of radial position, contrasting their MeHA counterparts, suggesting the presence of an inter-microgel shear stress at high shear rates. The factors governing inter-microgel mechanics are the microgel yield stress, which is a function of intrinsic microgel material properties, and AC bond density. To quantify these factors, we probed microgel pack mechanics using bulk rheology and surface mechanics using atomic force microscopy (AFM) on bulk HA hydrogels.

[089] *Rheological characterization of AC microgel packs*

[090] We first performed oscillatory rheology to measure the elastic storage modulus, G', and the loss modulus, G'', of each AC microgel condition (**Fig. 5**a). For all AC concentrations, G' was frequency-independent and greater than G'', indicating dominantly solid-like behavior at low strain. Further, we observed minimal changes in low-strain mechanical properties with increasing AC concentration, which is expected due to the molar ratio of DTT being much larger than that of the AC (see Methods). We then performed unidirectional rheology on the AC microgels and found that bare and low AC microgels to behave as Herschel-Bulkley (HB) yield stress fluids (Fig. 14a). At low shear rates, $\dot{\gamma}$, HB materials display a plateau in shear stress,

denoted as the material yield stress, σ_y, and high shear rates showcase constant, sub-Newtonian flow, where $\sigma \sim \dot{\gamma}^{<1}$. In contrast, medium and high AC concentration microgels do not have the characteristic plateau at low shear rates and can often display slip-like events, indicated by gradual increase followed by a rapid decrease in σ (Fig. 14b). Shear stresses at a given single shear rate can also vary up to half an order of magnitude (Fig. 5b).

[091] We repeated the oscillatory and unidirectional characterization of bare HA microgels from different MeHA stocks and microgel fabrications to quantify the effect of sample preparation error on microgel rheological properties (Fig. 14a,c). The measured G' and σ_y vary by less than a factor of 2, which is much less than the 5-fold change observed in σ_y for medium and high AC concentrations (Fig. 5b). Thus, we attributed the small variation in bare HA microgel rheological properties to errors in sample preparation. From previous works, we demonstrated that microgels display the linear scaling relationship, $G' \sim \sigma_y$ [16]. This relationship was leveraged to both account for sample preparation error, as changes in G' would be reflected in σ_y, and to isolate the effect of AC bonds on flowability. For a given sample, we normalized σ from unidirectional rheology by its respective average G' from oscillatory rheology (Fig. 5a) resulting in the expression, $\sigma/\langle G'(\omega)\rangle_\omega$, where ω is frequency, and plot the average calculated values (n=3) in Fig. 5b with error bars corresponding to the minimum and maximum shear stress at each shear rate.

[092] These normalized data confirm the classification of the bare and low AC microgels as HB materials, where forced flow in these microgel packs generates measured σ_y on the order of 10% of G' and with minimal variation in σ for all shear rates. In fitting the bare and low AC microgels to the HB model, we found that the magnitude of the power-law increase in σ at high $\dot{\gamma}$ decreased with increasing AC concentration (**Table 1**). The trend of decreasing power-law with increasing AC concentration continues with the medium and high AC samples, suggesting that flow becomes less Newtonian and more solid-like. However, the aberrant unidirectional rheology flow profiles for medium and high AC concentrations suggest that inter-microgel AC bonds are playing a larger role than the microgel yield stress during injection. We expect the maximum shear stress during microgel rearrangement to correspond to the bare microgel yield stress, however, AC bonds connecting microgels must break prior to microgel yielding for this to be true. We therefore sought to quantify the maximum shear stress arising from microgel rearrangement, and exposed to cellular cargo, by applying an instantaneous step-shear to our HA-AC microgel formulations and measuring their relaxation moduli, G'_r (Fig. 5c,d). We quantified the peak relaxation modulus, $G'_r(0)$, normalized by the samples' respective average G' from oscillatory rheology and observed an Increasing maximum shear stress with increasing

AC concentration (Fig. 5c). The peak relaxation moduli of the bare and low AC microgels were statistically indistinguishable, and their magnitude closely matches the bare microgel yield stress, corroborating our expected result. In contrast, instantaneously applied shear on high AC microgels can result in shear stresses up to five times the bare microgel yield stress. The values of peak relaxation moduli in medium and high AC microgels far exceed the bare microgel yield stress, suggesting yielding and microgel rearrangement is set by the strength of inter-microgel AC bonds instead of the microgel yield stress.

[093] Examination of G'_r over time, t, reveals a power-law relationship (Fig. 5d). Fitting these curves to the equation, $G'_r(t) = t^{-\beta}$, where β is the slope of the relaxation curve on a log-log scale, reveals increases in the magnitude of β with increasing AC concentration (Table 1). While the mechanism behind this scaling law requires further study, we attribute this feature to an increased rate of AC bond re-formation, likely due to increased AC bond density, after large shear events.

[094] To collectively explain the data, we hypothesize that low AC concentrations enable the microgels to ease rearrangement during flow, protecting cellular cargo better than their bare microgel counterparts. This hypothesis is supported by the observation of a lower power scaling between σ and $\dot{\gamma}$ (Table 1). However, when AC bond density increases above a certain threshold, the stress required to break bonds at the microgel-microgel interface is greater than the microgel yield stress, driving large-scale rearrangement, which causes aberrant flow profiles and increases the frequency of slip-like events that can damage cellular cargo.

[095] *Quantifying the stress to break AC bonds*

[096] We performed atomic force microscopy (AFM) on bulk HA-AC hydrogels with an adamantane-functionalized probe (see Methods) to and quantify the stress required to break AC bonds (**Fig. 6**a). Indentations on the same hydrogels were performed with a bare probe to quantify non-specific adhesion. Bulk hydrogels were prepared under the same conditions and at the same AC concentrations as their microgel counterparts (see Methods). The contact and detachment point were identified for each indentation curve and are denoted by the origin and open black circle respectively (Fig. 6b). The approach curve (red) is used to calculate elastic modulus, E, and the retraction curve (blue) is used to calculate adhesive work, W_a, and maximum adhesion force, F_a (Fig. 6b, see Methods). To calculate E, we fit the approach curve to the conical indentation variant of the Hertzian contact model given by the equation, $F = \frac{2E\tan(\alpha)d^2}{\pi(1-\upsilon^2)}$, where F is the force bending the cantilever, d is the cantilever displacement, α is the half-angle of the pyramidal probe, and υ is Poisson's ratio, which is measured separately to be 0.45 and is comparable to previous reports[33,34] (Fig. 15). We input the measured hydrogel υ and

manufacturer reported cantilever α as constants into the conical Hertzian contact model and found that fitting for a single variable, E, generates curves that fall directly on top of the measured data (Fig. 6c). Further, we found agreement between fitted values of E from the AFM data and predicted values of E using the equation, $E = 2G'(1 + \upsilon)$, and measurements of υ and G' (Fig. 6d – black dotted line). The data also showed that increasing AC concentration did not increase the calculated values of E, consistent with our rheological findings.

[097] We found measurements of W_a and F_a to fall within the noise floor of the measurement for indentations performed on AC hydrogels with a non-functionalized gold-coated probe (Fig. 16a). We then functionalized a gold probe with adamantane and repeated indentations on bare HA hydrogels. The calculated values of W_a and F_a fell within the measurement noise floor, indicating that non-specific adhesion between HA and adamantane is not present under the conditions tested here (Fig. 16b). Confirmation of the absence of non-specific adhesion allowed us to repeat AFM measurements on the HA-AC hydrogels with the adamantane functionalized probe to quantify AC adhesion strength. We found that both the magnitude of F_a and the distance from the indentation peak increased with increasing AC concentration (Fig. 16b).

[098] This observation indicated that larger forces acting over a larger distance were required to separate AC bonds between the probe and hydrogel. To account for both, we calculated W_a and found that it increased with increasing AC concentration (Fig. 6e). Dividing F_a by the calculated probe contact area, A_p, we quantified the stress generated during AC bond breaking and a similar trend in W_a (Fig. 6f). Input adamantane concentrations for probe functionalization were chosen to ensure that the limiting factor in AC bond engagement is cyclodextrin density on the hydrogel (see Methods). Since only half of the AC molecules are engaged during these experiments, we assume that the stress required to break these bonds would be double this magnitude between AC microgels. Thus, to compare the magnitude of the yield stress to the magnitude of the stress generated during AC bond breaking between microgels, we compared the data in Fig. 6f to half the bare microgel yield stress. Strikingly, we find the adhesive stress of the low and medium AC concentrations straddle the microgel yield stress line, supporting the hypothesis that breaking bonds in medium and high AC concentration microgels require stresses larger than the bare microgel yield stress. This conservative approximation further supports the idea that a balance between two forces dictates injectability and cell survival in granular guest-host microgels.

[099] To further establish that the relationship between inter-microgel adhesion and bulk microgel rheological properties dictates cell viability, we acted on an observation we made during microgel fabrication: the buffer used to wash the microgel particles strongly influences inter-particle adhesion. Specifically, microgels washed with PBS aggregate and have smaller

median diameters than their PBS/Tween 20-washed counterparts (Fig. 17a,b). This phenomenon has been reported previously and attributed to retention of Span 80 coatings[26]. Correspondingly, microgels washed with PBS only supported lower rates of NSC viability at the highest shear rate, decreased shear modulus and yield stress, and higher W_a (Fig. 17c – f), resulting from a thin layer of surfactant altering the microgel-microgel and microgel-cell interface.

[0100] Discussion

[0101] Here we quantified the mechanical forces imposed on cellular cargo in granular injectables and determined that a balance between bare microgel yield stress and AC bond strength dictates fluidity and thus cell viability. We demonstrated that granular HB yield stress fluids protect cellular cargo from shear stress. In unidirectional microgel rheology, we observe shear stresses on the order of 100 Pa at just 100 s^{-1}, which is below the minimum shear rate tested here. Based on previous literature and the MeHA control performed here, shear stresses of these magnitudes should be sufficient to induce cell death. However, we observe shear protection that facilitated 70% viability at shear rates two orders of magnitude above the maximum tested rheological shear rate. This result suggests the shear stress is dominantly generated at the needle wall during injection and shear protection extends into the sub-Newtonian flow regime.

[0102] With increasing shear rate, however, we found that the lack of inter-microgel interactions in bare HA microgels resulted in reduced cell viability. The increased cell death could be due to an increased velocity gradient or increased frequency of microgel rearrangement at high shear rates. Physical dislocation of microgels could either expose more cells to needle wall shear stresses or could impose compressive stresses on the cellular cargo. We show that greater cell viability is achieved with low concentrations of AC, where inter-particle crosslinks decrease the rate of shear stress generation with increased shear rate. We further identified that in order to break AC bonds between microgels at low AC concentrations, shear stresses less than the bare HA microgel yield stress is required. This feature would ensure that in the event of microgel rearrangement AC bond breaking would be reinforced by microgel jamming, allowing new AC bonds to form as microgels rolled past one another. Above the AC concentration that requires stresses higher than the microgel yield stress to break AC bonds, a microgel rearrangement event would not be supported by jamming, resulting in large microgel dislocations and subsequent shear stress magnitudes that far exceed those required to damage the cellular cargo.

[0103] We anticipated a linear relationship between AC molecule to HA-monomer repeat unit and work of adhesion, and for additional AC bonds to behave as an increased number of elastic spring elements per unit area. However, we found that 5- and 10- fold increases the AC molecule to HA-monomer repeat unit ratio between the low-med and low-high AC

concentrations respectively resulted in 2- and 5- fold increases in the calculated work of adhesion. We also observed the distance at which the probe detached from the sample increased with increasing AC concentration. The non-linear relationship between molar ratio and work of adhesion coupled with the observation that retraction increasingly extends beyond the original contact point with increasing AC concentration suggests that the HA within the microgel is strained prior to AC bonds breaking. This finding indicates that internal microgel stiffness can also play a large role in granular injectable systems utilizing AC interactions and suggests that microgels can deform and store energy as AC bonds are strained. This is a crucial finding, not only to our work, but also for understanding the effect of AC bonds on the field of granular injectables, which have documented cell viability dependence on microgel geometry[22]. Engagement of more AC bonds, whether it be through increased contact area due to changes in microgel size and geometry or AC density, leads to a non-linear elastic response whose mechanics depend heavily on yielding and intra-microgel properties.

[0104] The invention was facilitated by a 3D printing-based method to screen our shear-protecting injectables, where the ability to control and observe the spatial distribution of cells during injection enabled exploration of the interplay between inter-particle adhesion and microgel yield stress on shear protection and cell viability. This platform has utility in fine-tuning other granular injectables for a host of regenerative medicine applications with alternative target tissues, such as cell replacement for myocardial infarction (MI) and type-I diabetes[22,35,36]. This platform can also be used to tune injectability, shear-protection, and intra-tissue retention independently without making major modification to the injected 3D matrix itself, providing applications that require the injectable to pass through an adapter with a diameter change, generating extensional flow.

[0105] Cell culture

[0106] Murine neural stem cells (NSCs) isolated from the cortices of embryonic day 15 – 18 C57/BL6 mice were obtained from Sigma Aldrich (SCR029). NSCs were cultured according to manufacturer protocols. Briefly, tissue culture dishes were coated with 20 ug/mL poly-ornithine and 10 ug/mL laminin stepwise overnight. Mouse NSC expansion media (Sigma Aldrich, SCM008) was used to culture NSCs on the coated tissue culture dishes and to swell the microgels. NSCs were cultured at 37 ^{o}C and 5% CO_2 in 2D where half-media changes were performed every other day until reaching 80 – 90% confluency. To ensure effects of nutrient depletion are minimized during 3D microgel culture, experiments extending beyond 24 h were supported by 50% daily media exchanges.

[0107] Methacrylation of Hyaluronic Acid (HA)

[0108] Methacrylated hyaluronic acid (MeHA) was prepared as described previously[24,25].

Briefly, HA (Lifecore Biomedical, part no. HA60K-5) with a nominal molecular weight of 60 kDa was suspended in deionized water at a maximum of 1 % (w/w). The solution was continually stirred, placed on ice for the remainder of the reaction, and 8 mL of methacrylate anhydride (part no) per gram of HA was added dropwise (approximately 10-fold excess relative to the disaccharide repeat unit). The pH was maintained between 8 – 9 using NaOH for 6 – 8 h. The reaction is continued overnight at 4°C to achieve ~95% functionalization. To collect the MeHA, chilled ethanol was added in ten-fold excess to the solution causing the MeHA to precipitate out. The mixture was centrifuged, ethanol was aspirated, and the MeHA was resuspended in deionized water. The resuspended MeHA was vacuum filtered through a 0.22 um mesh to remove unreacted methacrylate anhydride. The solution was stored at -80°C overnight and lyophilized for long-term storage.

[0109] Microgel fabrication and functionalization

[0110] To fabricate HA microgels, we crosslinked hydrogel droplets in an inverse emulsion. The aqueous phase consists of 2% (w/w) MeHA and crosslinker 1,4-Dithiothreitol (DTT) with a 0.7 thiol:HA monomer repeat ratio and the organic phase consists of kerosene and 1.25% (w/w) Span-80 (Sigma Aldrich, S6760-250ML). The concentrations of each component in the aqueous phase were determined by fabricating bulk hydrogels and performing oscillatory rheology, where we chose parameters that generated hydrogels with 400 Pa storage moduli to mimic the mechanical properties of the brain parenchyma (Fig. 8b). The resulting solution was homogenized using the Bio-Gen PRO200 (Pro Scientific, 01-01200) to create smaller and more monodisperse emulsion droplets. The Michael Addition reaction was performed by mixing on ice for 4 h. Once crosslinked, the organic phase can be removed from the mixture. To rid of excess kerosene and surfactant, the microgels were serially washed with 0.1% (v/v) Tween 20 in PBS (Sigma Aldrich, P1379-25ML). Wash steps are performed by diluting the product by a minimum of a factor of 1000 (v/v) for each wash.

[0111] Inter-microgel adhesivity was tuned using a custom adamantane peptide (Adamantane-KKKCG) and cyclodextrin (Tocopharm, part no. 81644-55-5) (AC) guest-host system, where reported concentrations of each are approximated based on the calculated 95 – 100 % methacrylation efficiency from ^{1}H-NMR and assuming random close packing of microgels that yield a 64% solid fraction. The pelleted microgels were incubated with AC for a minimum of 2 h before use. Adamantane and cyclodextrin are added to the microgel pellet stepwise in equivalent molar ratios, where reported concentrations of 0.01, 0.05, and 0.11 correspond to the individual guest or host molecule to HA monomer repeat unit ratio. Thus, we approximate that 2, 10, and 22% of the HA repeat units bear AC molecules. These concentrations were chosen as the methacrylation protocol used here yields 95 – 100% efficiency and 70% of the HA repeat

units are used for DTT crosslinking. The remaining 25 – 30% of available methacrylate groups for AC provided a sufficient dynamic range of rheological properties for this HA-DTT concentration. The same procedure was used to functionalize microgels with integrin binding peptide (Anaspec, part no. AS-62349).

[0112] Rheology

[0113] To characterize the mechanical properties of the microgel packs, we performed oscillatory, unidirectional, and step-strain rheology on an Anton Paar 302 rheometer with a 25 mm plate-plate configuration and 1 mm gap. We centrifuged microgel samples at 4000 $\times g$, removed the liquid supernatant, and pipette-mixed before loading onto the rheometer. Oscillatory rheology used throughout all studies applied a 1% strain across frequencies ranging between 10^{-2} and 10^{2} Hz. Unidirectional rheology was performed between shear rates of 10^{-2} and 10^{3} s^{-1} and the results are fit to the Herschel-Bulkley (HB) model, $\sigma = \sigma_y(1 + \left(\frac{\dot{\gamma}}{\dot{\gamma}_c}\right)^p)$, where σ is the measured stress response, σ_y is the yield stress, $\dot{\gamma}$ is shear rate, $\dot{\gamma}_c$ is the critical shear rate at which the stress response changes from solid- to fluid-like and p is the flowability of the material at high shear rate (Table 1). To determine the stress relaxation capabilities of the AC microgels, we applied a 50% step-strain and measured the stress response and fit the curves to the power-law model, $G'_r(t) = t^{-\beta}$. The high AC microgels appear to have two power-law regimes, and we only report the fitted β for the first here.

[0114] Table 1. Fitted values for rheological characterization in Fig. 5b,d.

[AC]	σ_y	$\dot{\gamma}_c$	p	β
bare	0.06	6.60	0.49	0.07
low	0.07	10.53	0.43	0.12
med	-	-	0.36	0.15
high	-	-	0.29	0.27

[0115] Unidirectional shear was also employed to determine 15 – 60 mg/mL MeHA viscosity as a function of shear rate (see Supplementary Information, Fig. 8a). We found viscosity to increase with MeHA concentration and all concentrations have a slight shear rate dependence. Further examination of shear stress measurements in these experiments reveals a linear dependence between shear stress and shear rate ($\sigma \sim \dot{\gamma}$) at high shear rates, which is a property of Newtonian flow.

[0116] AFM on HA hydrogels

[0117] HA hydrogels were prepared by pipette mixing 2% (w/w) MeHA and 0.7 molar ratio DTT. 20 uL droplets were placed on polystyrene tissue culture dishes and immediately submerged in kerosene with 1.25% (w/w) Span80 to mimic the inverse-emulsion microgel

synthesis. Samples were crosslinked for a minimum of 4 h. The organic phase was removed from the tissue culture dish and the samples were washed with PBS or PBS and 0.1% (v/v) Tween 20. The hydrogel droplet was left to swell in PBS overnight. Similarly, AC was added stepwise overnight. The AC solutions were removed before performing AFM.

[0118] Force measurements were performed on a MFP3D-BIO (Oxford Instruments) AFM using gold-coated pyrex-nitride probes (NanoWorld, PNP-Tr-AU) with nominal spring constant 0.08 N/m. Each probe was calibrated before use by the thermal method. A force trigger threshold of 1- 5 nN was used, and indentation depth was limited to 2 μm. All measurements were performed in PBS at room temperature. In fitting the approach curve, E is constrained to 0.1 – 5 kPa. Adamantane-functionalized probes were made using published protocols[37]. In brief, gold-thiol reactions were performed by gently submerging the gold-coated probe in 1 mM adamantane solution overnight, then rinsing with several mL deionized water before use. We anticipate a much higher adamantane density on the functionalized gold probes than on any of the adamantane-functionalized microgels, as the gold-thiol chemistry is expected to generate a higher adamantane density than the relatively inefficient thiol-methacrylate Michael addition. Further, the adamantane concentration used to functionalize the probe is much higher than the highest working concentration of 0.2 mM used to functionalize the microgels, where the thiol is a limiting reagent. We therefore assume that the factor limiting adhesion in AC bond engagement is the cyclodextrin density on the hydrogel, rather than the adamantane density on the functionalized probes.

[0119] To calculate adhesive stress, we determined the peak adhesive force upon probe retraction, F_a. This value was divided by the maximum contact area, A_p, which we calculated based on the maximum identified probe penetration depth.

[0120] Printing Preparations

[0121] To facilitate fluorescence imaging and assaying of various shear rates within one sample preparation process, we pipetted 75 uL of microgels prepared at 1 $\times g$ and up to 75 uL of liquid media are pipetted into in glass bottom 96-well plates. To ensure the microgels settled to the bottom of the well, they were gently agitated and incubated at 37 ^{o}C for 10 minutes. When the NSCs reached 80 – 90% confluence, we removed the cells from the tissue culture dish by incubating with Accutase for 5 minutes. The cells in solution were placed in a 15 mL centrifuge tube and centrifuged at 200 $\times g$ for 5 minutes. The Accutase was aspirated, and the cell pellet was diluted to achieve the desired cell density. NSCs were gently pipette-mixed into MeHA or HA microgels that were centrifuged at 4000 $\times g$ for 5 min. The resulting solution of MeHA or HA microgels with NSCs was loaded into the back of a 100 uL Hamilton gas-tight syringe. The plunger was slowly pushed through the syringe until the solution reaches a 30G luer-lock affixed

to the syringe. Before injection through the needle, we loaded the syringe onto the 3D printer, where the pump velocity was set to the lowest experimental flow rate. We jogged the pump until a small sphere of cells and matrix form at the needle tip.

[0122] Cell Viability Measurements and Calculations

[0123] Cell viability was determined using the Live/Dead assay (Thermo Fisher, L3224) following manufacturer protocols. Live/dead images were acquired using a Zeiss LSM 710 confocal and images intended to perform feature size measurements are acquired using a Nikon TE2000-E epifluorescence microscope. We calculated cell viability manually isolating the central plane of the printed feature within a 3D confocal z-stack. We approximated live and dead cells to occupy the same area within a given plane and performed viability calculations with the equation $\% \; viability = \frac{live\ cell\ area}{total\ cell\ area}$. To determine total cell area, each channel was thresholded using Otsu's method and the binary images were added together. Co-localization of the red and green channel was determined to be indicative of compromised cell membranes and excluded from the live cell population. Thus, we calculated live cell area by subtracting the binarized dead cell channel from the live cell channel. Small fragments of cells can remain from this calculation, so we eliminated areas smaller than 50 um^2 before calculating the live cell area. We validated this approach using the equation, $\% \; viability = \frac{\#\ live\ cells}{\#\ total\ cells}$, for the microgel injectables where single cells are easily identifiable due to low cellular volume fraction and find agreement between the two methods (Fig. 18).

[0124] Injection into HA hydrogels and calculations from 3D confocal images

[0125] Much like the preparation of samples for AFM, we cast 100 uL of 2% MeHA hydrogels with a 0.7 DTT molar ratio onto 3 cm tissue culture dishes and submerged them in kerosene to prevent evaporation and to mimic the microgel fabrication protocol used here. The samples were crosslinked for 4 h before removing the kerosene and washing with PBS and 0.1% Tween 20. We allowed the samples to swell in PBS overnight before injecting 1 uL mixtures of NSCs and HA microgel or liquid media at a flow rate of 360 uL/h, corresponding to our lowest tested shear rate of 250 s^{-1} (Fig. 5a). The injections were performed by loading the mixtures into our 3D printing syringe and lowering the needle into the hydrogel at 0.1 mm/s to a depth of 0.5 mm from the culture dish bottom. We removed the needle at the same low velocity to minimize damage or displacement of the injected material. Injected NSCs were cultured in this hydrogel for 24 h before introducing 4 mM calcein-AM for 4 h to visualize cells encapsulated in the retained volume, which was measured with confocal microscopy.

[0126] Imaging was performed with a 10x objective with a NA of 0.45, where the sampling frequency in the X-Y plane is 1.66 um and 8.31 um in the Z-plane. Due to the difference in

sampling frequency between the X-Y and Z planes, we interpolate and re-sample data along the Z-axis to create cubic voxels. We perform morphological transformations to fill the gaps between cells, and calculate the total volume occupied by the binary image (see Supplementary Information, Fig. 19). For data showing protrusion depth in Fig. 2, we identify the minimum and maximum z-position manually within the re-sampled 3D stack with detectable fluorescence. The minimum z-position, corresponding to the glass bottom, is designated to be z = 0 um and the maximum z-position with detectable fluorescence across all RGD concentrations is determined to be 420 um above the glass bottom. The fluorescence data is masked on a slice-by-slice basis, where data falling at z = 0 um is given a grayscale value of 1 and data falling at z = 420 um is given a grayscale value of 255. Data falling on slices between the minimum and maximum z-position is designated an intensity value between 1 and 255 based on its respective z-position. We then take the maximum intensity projection of the 3D stack to identify maximum z-depth of protrusion formation as a function of RGD concentration and time.

[0127] Supplementary Information

[0128] HA microgel size quantification

[0129] We crosslink HA microgels with DTT in the aqueous phase of an inverse emulsion. Residual methacrylate groups remain after crosslinking, which is confirmed by the functionalization of these microgels with a fluorescently labeled cysteine (FITC-cysteine) (Fig. 7a). We quantify the size distribution of these microgels by measuring the fluorescent area of each microgel and calculate their respective diameters using the equation, $d_A = \sqrt{\frac{4A}{\pi}}$. The probability density function (PDF) of the size distribution can be seen in Fig. 7b, where we see a relatively monodisperse population of microgel spheres with a characteristic median diameter of 9.95 um.

[0130] Using MeHA viscometry to predict shear stress during injection and HA microgel rheology with increasing centrifugation force

[0131] We perform unidirectional rheology to measure the viscosity of our microgel precursors, MeHA, which acts as a viscous Newtonian liquid control for our shear protection experiments (Fig. 14a). We observe small decreases in viscosity at low shear rate and Newtonian fluid-like behavior, where $\sigma \sim \dot{\gamma}$, at higher shear rates. Since the shear rates tested fall within the Newtonian-like regime, we can approximate shear stress using the equation for Hagen-Poiseuille flow through a pipe with circular cross-section, $\sigma_w = \frac{4Q\mu}{\pi R^3}$, where σ_w is the maximum shear stress at the needle wall, μ is the solution viscosity, and R is the needle radius. Using the viscosity evaluated at 250, 1250, and 4125 s^{-1} from unidirectional rheological characterization (Fig. 8a), we predict the respective σ_w to be 5, 30, and 100 Pa for 3% (w/w) MeHA. The

maximum shear rate chosen corresponds to the maximum linear velocity of the pump used for our 3D printing experiments and the concentration of HA was chosen based on the viscosity required to achieve shear stresses similar to those observed to damage cells in the literature[30,31].

[0132] Based on previous HA hydrogel works[24], we choose to formulate microgels using HA and DTT crosslinking concentrations of 2% (w/w) and 0.7 thiol-to-HA monomer ratio to mimic the mechanical properties of the brain parenchyma. While a single HA and DTT concentration combination is chosen for the work here, we demonstrate a secondary level of control over their mechanical properties by increasing the centrifugal forces we prepare them at to increase elastic modulus, G'. We performed small-strain oscillatory rheology on HA microgels at various centrifugal forces and compared their moduli to their bulk hydrogel counterpart (Fig. 8b). We found that the microgels asymptotically approach the bulk hydrogel modulus with increasing centrifugal force.

[0133] NSC-HA microgel interaction

[0134] HA microgels are functionalized with 0.2 mg mL^{-1} RGD and mixed with NSCs. These mixtures are incubated, where NSCs migrate and coalesce into spheroids. These spheroids extend protrusions and interact with the surrounding microgel matrix before forming network spanning structures, such as those seen in Fig. 2 (Fig. 9).

[0135] NSC dispersal with free-RGD control

[0136] NSCs are dispersed in liquid media and ambient RGD to quantify aggregate and network formation at the untreated glass interface without the presence of microgels. We vary the RGD concentration from 0.02 – 1.0 $mgmL^{-1}$. Cells appear to aggregate over the 24 h experiment, similar to their morphology in bare HA microgels in 3D. With increasing RGD concentration, we observe increased rates of cell death (red, Fig. 10).

[0137] 3D printing feature size predictions and issues arising with cell-laden MeHA printing

[0138] We sought to determine the cause for the irregularly shaped NSC laden MeHA structures during injection into HA microgels (Fig. 4a). Previous works have shown that printed feature diameter can be predicted using a form of the continuity equation, $Q = vA$, where we show A is a circular cross-sectional area of diameter, d, given by $A = \pi\frac{d^2}{4}$ [16]. Using this equation, we print 3 mm lines at translational velocities between 0.05 – 0.22 mm/s and flow rates between 25 – 225 uL/h to yield predicted feature diameters, d_p , between 200 – 1200 um. We first demonstrated that the NSC-laden (Fig. 4) and 1 um particle-laden (Fig. 11a) microgel injectables generate features with constant cross-sectional areas and measured diameters, d_m, that align

well with our predictions (Fig. 11c). NSC-laden MeHA injectables, however, generate unpredictable diameters across this same range of printing parameters (Fig. 11b).

[0139] To determine if the cause for unpredictable NSC + MeHA features are due to the HA microgel support bath, we fabricated an alternative polyethylene glycol- (PEG) based microgel support bath. We performed a free-radical polymerization in the aqueous phase of an inverse emulsion, where the aqueous phase consisted of 25% (w/w) PEG acrylate (PEGa), 1.5% (w/w) PEG diacrylate (PEGda), 0.15% (w/w) ammonium persulfate (APS) and 0.15% (w/w) TEMED. The solution is placed on ice, purged with nitrogen, and stirred for 4 h. We then confirm complete crosslinking of the microgels and absence of residual acrylate groups by mixing them with FITC-cysteine. We observed absence of fluorescence, indicating we have fabricated microgels that act as a biologically inert and charge neutral alternative to their HA microgel counterparts. Printing MeHA and particle mixtures into the PEG microgels, we find d_m slightly exceeds d_p, suggesting that diffusion of MeHA into the pore space between PEG microgels or differential osmotic pressure can cause the injected material to expand. Nonetheless, features appear to closely follow our predictions suggesting poor feature size predictability is not due to MeHA alone or the HA microgel support bath.

[0140] In concluding that unpredictable diameters of the NSC + MeHA injections is not due to material interactions, we compared the predicted and measured diameters of the NSC + MeHA prints and found that d_m was constant for all d_p across the vast range of printing parameters used here (Fig. 11b,c). Further, most d_m fall between 100 – 200 um (Fig. 11c) which would fall on the same order as the inner diameter of our 30G printing needle (I.D. = 160 um, dotted line). From these observations, we attributed the discrepancy between d_m and d_p to cells settling in the syringe during printing and fragmentation of the NSC-MeHA mixtures upon exiting the needle. In these injections, the inner diameter of the needle sets the printed feature size. This finding further emphasizes the need to avoid hydrogel encapsulation approaches where cell settling cannot be ignored during formulation.

[0141] Determining the timescale associated with shear stress induced death

[0142] To determine the timescale associated with shear stress-induced cell death, we perform cell viability assays on mixtures of NSCs and MeHA printed at shear rates of 250, 1250, and 4125 s^{-1} at 6, 24, and 72 h after printing. We find cell viability for each condition to be greater than 75% at the 6 h timepoint (Fig. 16a-c). Viability decreased between the 6 and 24 h timepoints, however, we do not find significant decreases in viability between 24 and 72 h. As a result, shear induced cell death experiments shown in the body of the paper are from the 24 h timepoint.

[0143] Isolation of shear stress as the dominant variable contributing to cell death

[0144] While HA crosslinked with DTT is widely used as a 3D culture platform and AC have shown to be non-cytotoxic[5,22], means of fabrication, microgel geometry, and decreases in transport could also play role in cell viability. To establish baseline viability of NSCs in culture, we first dispersed 0.5M NSCs into 1 mL liquid media and stored them in gas-tight cryovials to reduce evaporation for up to 7 d. Low cell numbers in large volumes of media in these conditions allowed us to isolate the effects of nutrient consumption on cell viability. Further, we stored the cryovials at 4 °C, 25 °C and 37 °C to vary the metabolic activity of the cells (Fig. 13a) . Media in the 25 °C and 37 °C conditions is treated with 25 mM Hepes buffer to ensure pH stability in the absence of incubation with 5% CO_2. We found that viability surpassed the 70% benchmark in liquid media for 5 d when stored at 4 °C, but not for those stored at 25 °C or 37 °C (Fig. 13b). This finding led us to hypothesize that, consistent with previous reports, nutrient consumption and metabolic activity are incubation temperature dependent[38].

[0145] Dispersals were repeated with 0.5M NSCs into 1 mL microgel media at 4 °C to reduce the effects of low viability due to increased metabolism and to isolate potential negative effects of 3D microgel culture. We found that viability rapidly decreased between day 3 and 5 and hypothesized that cell density could be playing a role in cell viability. In contrast to their liquid media cultured counterparts, NSCs are suspended in 3D, where cell-cell chemotactic signaling and contact with neighboring cells could be impaired by greater initial distances between cells (Fig. 13a). Further, manufacturer protocol reports low viability at low cell densities even in 2D. Thus, we increased the input cell density up to 20 M cells/mL and found that cell viability increases with increasing cell density in microgels, and the highest cell density surpasses 70% viability for up to 5 d.

[0146] We leveraged these data to set our cell density during injection experiments. While we sought to minimize cell density to preserve the shear protecting capabilities of microgels, we also sought to achieve cell densities that promoted the highest viability. We therefore chose to print with cell densities of 20 M cells/mL, where we approximate the cellular volume fraction to be 10 – 15 % assuming a cell diameter of 12 um. In order to counteract the higher metabolic rates of cells in our 3D culture experiments, daily 50% media exchanges are performed.

[0147] Effects of batch-to-batch variability on microgel rheology

[0148] We observed large variations in the unidirectional rheology for medium and high AC concentration microgels. To ensure that these erratic data were not due to variation in methacrylation between MeHA, we first repeated MeHA functionalization and fabricated microgels using the second MeHA stock. With the microgels fabricated using the second MeHA stock, we prepared two separate microgel samples by centrifuging them at 4000 $\times g$. Unidirectional rheology curves from these two samples (black and blue data, Fig. 14a) are

compared to the microgels fabricated from the first MeHA stock and prepared at 4000 $\times g$ (red data, Fig. 14a), where we see less than a factor of 2 change in the shear stress plateau, σ_y, at low shear rate. Contrasting these data to the 5-fold change in σ_y for the medium and high AC concentration microgels (Fig. 5b), we attribute this difference to errors in sample preparation.

[0149] To further demonstrate that AC bonds are driving the erratic flow properties of medium and high AC concentration microgels, we examined single representative curves of the two (Fig. 14b). In contrast to their bare microgel counterparts in Fig. 14a, medium and high AC concentration microgels do not display a clear plateau at low shear rate, but instead showcase constant sub-Newtonian flow with occasional slip-like events, where briefly decreases after a period of rapid increase.

[0150] To further corroborate that small changes in the measured σ_y can be attributed to sample preparation errors, we performed oscillatory rheology on the same samples from Fig. 14a. Much like the σ in the unidirectional rheology data, variation in G' falls within a factor of 2 for all AC (Fig. 14c). These results demonstrate repeatability in the protocol established here, and that unfavorable flow properties of the medium and high AC concentration microgels are a property of their respective systems.

[0151] Measuring Poisson's Ratio for HA hydrogels

[0152] Samples for measuring Poisson's Ratio, υ, are prepared by punching 8 mm disks from the 25 mm diameter x 1 mm thick rheological hydrogel sample in Fig. 8b (Fig. 15a-b). The smaller diameter disks are loaded onto the rheometer, the 25 mm diameter probe is lowered until contacting the sample, and 100 um compressive displacements are applied up to 500 um total displacement (50% compressive strain). We calculate Poisson's Ratio using the equation $\upsilon = \frac{\varepsilon_t}{\varepsilon_a} = \frac{\frac{\Delta D}{D}}{\frac{\Delta h}{h}}$, where ε_t is the transverse strain arising from axial strain, ε_a, and can be measured by examining changes in diameter, D, changes with applied changes in height, h. The measured values for υ can be seen in Fig. 15b, where the distributions of calculated values five displacements on the same sample are shown and the dotted line represents the cumulative mean of all measurements.

[0153] Indentation with bare and adamantane-functionalized probes

[0154] We fabricated hydrogels with the AC concentrations used herein. We performed AFM on these hydrogels with a bare probe and found that the force measurements on the retraction curves seldom dipped below $F = 0$ nN, indicative of minimal probe-hydrogel adhesion (Fig. 16a). In contrast, indentations performed with an adamantane-functionalized probe displayed increasing adhesion with increasing AC concentration (Fig. 16b). As surface adhesion measurements heavily depend on probe longevity and we used the same adamantane-

functionalized probe for all of the HA-AC hydrogels, we performed two sets of measurements on each hydrogel. We performed the first set of indentations in order of increasing AC concentration and the second set of measurements in order of decreasing AC concentration. We did not observe significant changes between the two, and representative curves of each measurement on bare and high AC concentration hydrogels can be seen in Fig. 16c. Thus, we concluded that our probe functionalization and indentation protocol did not depend on order of indentation on the hydrogel samples.

[0155] Microgel wash comparison

[0156] Serial PBS wash steps can be performed to remove most of the kerosene and surfactant however, thin oily coatings can persist[26]. To rid of excess surfactant, we wash with 0.1% (v/v) Tween 20 (PT) before adding peptides or mixing with NSCs. However, during the fabrication process, we observe thin organic-phase coatings from PBS only washes promote microgel aggregation when examined under brightfield microscopy (Fig. 17a). We find that microgel diameters are relatively monodisperse (n = 100) and normally distributed with a mean diameter of approximately 10 um for Tween 20 washed microgels and 5 um for PBS only washed microgels (Fig. 17b). Consistent with results from high AC concentration granular injectables, we observe decreased cell viability in PBS only washed microgel at high shear rates (Fig. 17c). Rheological samples were prepared by centrifuging the microgels at 4000 $\times g$ for 5 min. During oscillatory rheology we find that G' is greater than G'' and the bulk elastic moduli are frequency independent for both washes (Fig. 17d). During application of unidirectional shear, we observe a plateau at low shear rate and sub-Newtonian flow ($\sigma \sim \dot{\gamma}^{<1}$) at high shear rate, characteristics of Herschel-Bulkley yield stress fluids (Fig. 17e). However, we observe a 2-fold difference in G' and σ_y between the two wash conditions. Further, unidirectional rheology of PBS washed samples can display the same slip-like events observe in high AC microgels (Fig. 14b) and result in lower cell viability when used as an injectable. We prepared bulk hydrogels washed with and without Tween 20 and performed AFM with a bare probe to find that samples washed in PBS alone generate higher values of W_a than their Tween 20 washed counterparts. The qualitative, rheological, and surface characterizations shown here suggest changes in free surface energy or surface tension due to residual surfactant. This property highlights the importance of the balance between intra- and inter-microgel properties and acts as a comparator to the AC system.

[0157] Live/dead calculation validation

[0158] Due to cellular aggregation during injection, single cells are difficult to identify in NSC-laden MeHA injections. Instead of calculating viability in these samples using the equation, $\%\ viability = 100\ x\ \frac{\#\ live\ cells}{\#\ total\ cells}$, we use $\%\ viability = 100\ x\ \frac{live\ cell\ area}{total\ cell\ area}$, making the

assumption of equivalent live and dead cell volumes. To validate this approach and confirm our assumptions, we calculate viability in the bare HA microgel injectables using the two methods (Fig. 18). Minimal changes are observed between the two calculations and the trend of increased cell death with increasing shear rate is preserved. Nonetheless we still acknowledge the magnitude of viability may vary when calculating NSC in MeHA viability, however, the images corroborate finding that MeHA underperforms microgel-based injectables and that high shear rates decrease viability well below the 70% target. Further, we anticipate that the approximation of equivalent live and the dead cell volumes deteriorates for increased rates of cell death. This conservative approach further highlights the improvements in viability when using microgel-based injectables.

[0159] Image processing to calculate retention volume, V_r

[0160] Images of injectable laden hydrogels are taken using confocal and are pre-processed to visualize the volume in real space (see Methods). We apply a Gaussian blur with a kernel half-width of 0.7 pixels before applying a threshold. Serial morphological transformations, dilation and erosion, are used to fill the gaps between cells on a slice-by-slice basis (Fig. 19). The resulting binary image is used to calculate the total number of voxels occupied by the injectable. These experiments are repeated (n=3) for both liquid- and bare HA microgel-based injectables. Reported values of retention volume, V_r, are normalized by the mean liquid V_r.

[0161] References

[0162] 1 Tan, H. & Marra, K. G. Injectable, biodegradable hydrogels for tissue engineering applications. *Materials* **3**, 1746-1767 (2010).

[0163] 2 Zhao, L., Weir, M. D. & Xu, H. H. An injectable calcium phosphate-alginate hydrogel-umbilical cord mesenchymal stem cell paste for bone tissue engineering. *Biomaterials* **31**, 6502-6510 (2010).

[0164] 3 Adil, M. M. *et al.* Engineered hydrogels increase the post-transplantation survival of encapsulated hESC-derived midbrain dopaminergic neurons. *Biomaterials* **136**, 1-11 (2017).

[0165] 4 Liu, Z. *et al.* The influence of chitosan hydrogel on stem cell engraftment, survival and homing in the ischemic myocardial microenvironment. *Biomaterials* **33**, 3093-3106 (2012).

[0166] 5 Gaffey, A. C. *et al.* Injectable shear-thinning hydrogels used to deliver endothelial progenitor cells, enhance cell engraftment, and improve ischemic myocardium. *The Journal of thoracic and cardiovascular surgery* **150**, 1268-1277 (2015).

[0167] 6 Liang, Y., Walczak, P. & Bulte, J. W. The survival of engrafted neural stem cells within hyaluronic acid hydrogels. *Biomaterials* **34**, 5521-5529 (2013).

[0168] 7 Tang, J. D., Roloson, E. B., Amelung, C. D. & Lampe, K. J. Rapidly assembling pentapeptides for injectable delivery (RAPID) hydrogels as cytoprotective cell carriers. *ACS Biomaterials Science & Engineering* **5**, 2117-2121 (2019).

[0169] 8 Aguado, B. A., Mulyasasmita, W., Su, J., Lampe, K. J. & Heilshorn, S. C. Improving viability of stem cells during syringe needle flow through the design of hydrogel cell carriers. *Tissue Engineering Part A* **18**, 806-815 (2012).

[0170] 9 DeForest, C. A. & Anseth, K. S. Cytocompatible click-based hydrogels with dynamically tunable properties through orthogonal photoconjugation and photocleavage reactions. *Nature chemistry* **3**, 925-931 (2011).

[0171] 10 DeForest, C. A., Polizzotti, B. D. & Anseth, K. S. Sequential click reactions for synthesizing and patterning three-dimensional cell microenvironments. *Nature materials* **8**, 659-664 (2009).

[0172] 11 Correa, S. *et al.* Translational applications of hydrogels. *Chemical Reviews* **121**, 11385-11457 (2021).

[0173] 12 Sharma, P. K., Taneja, S. & Singh, Y. Hydrazone-linkage-based self-healing and injectable xanthan–poly (ethylene glycol) hydrogels for controlled drug release and 3D cell culture. *ACS applied materials & interfaces* **10**, 30936-30945 (2018).

[0174] 13 Yang, J.-A., Yeom, J., Hwang, B. W., Hoffman, A. S. & Hahn, S. K. In situ-forming injectable hydrogels for regenerative medicine. *Progress in polymer science* **39**, 1973-1986 (2014).

[0175] 14 Grosskopf, A. K. *et al.* Injectable supramolecular polymer–nanoparticle hydrogels enhance human mesenchymal stem cell delivery. *Bioengineering & translational medicine* **5**, e10147 (2020).

[0176] 15 Moshaverinia, A. *et al.* Encapsulated dental-derived mesenchymal stem cells in an injectable and biodegradable scaffold for applications in bone tissue engineering. *Journal of Biomedical Materials Research Part A* **101**, 3285-3294 (2013).

[0177] 16 Morley, C., Kiwimagi, K., Tordoff, J., Weiss, R. & Angelini, T. in *APS March Meeting Abstracts.* K65. 002.

[0178] 17 Morley, C. D. *et al.* Quantitative characterization of 3D bioprinted structural elements under cell generated forces. *Nature communications* **10**, 3029 (2019).

[0179] 18 Highley, C. B., Song, K. H., Daly, A. C. & Burdick, J. A. Jammed microgel inks for 3D printing applications. *Advanced Science* **6**, 1801076 (2019).

[0180] 19 Ouyang, L., Wojciechowski, J. P., Tang, J., Guo, Y. & Stevens, M. M. Tunable microgel-templated porogel (MTP) bioink for 3D bioprinting applications. *Advanced Healthcare Materials* **11**, 2200027 (2022).

[0181] 20 Muir, V. G. *et al.* Sticking Together: Injectable Granular Hydrogels with Increased Functionality via Dynamic Covalent Inter-Particle Crosslinking. *Small* **18**, 2201115 (2022).

[0182] 21 Qazi, T. H. *et al.* Anisotropic Rod-Shaped Particles Influence Injectable Granular Hydrogel Properties and Cell Invasion (Adv. Mater. 12/2022). *Advanced Materials* **34**, 2270092 (2022).

[0183] 22 Widener, A. E., Duraivel, S., Angelini, T. E. & Phelps, E. A. Injectable Microporous Annealed Particle Hydrogel Based on Guest–Host-Interlinked Polyethylene Glycol Maleimide Microgels. *Advanced NanoBiomed Research* **2**, 2200030 (2022).

[0184] 23 Riley, L., Schirmer, L. & Segura, T. Granular hydrogels: emergent properties of jammed hydrogel microparticles and their applications in tissue repair and regeneration. *Current opinion in biotechnology* **60**, 1-8 (2019).

[0185] 24 Ananthanarayanan, B., Kim, Y. & Kumar, S. Elucidating the mechanobiology of malignant brain tumors using a brain matrix-mimetic hyaluronic acid hydrogel platform. *Biomaterials* **32**, 7913-7923 (2011).

[0186] 25 Marklein, R. A. & Burdick, J. A. Spatially controlled hydrogel mechanics to modulate stem cell interactions. *Soft Matter* **6**, 136-143 (2010).

[0187] 26 Qazi, T. H., Muir, V. G. & Burdick, J. A. Methods to characterize granular hydrogel rheological properties, porosity, and cell invasion. *ACS Biomaterials Science & Engineering* **8**, 1427-1442 (2022).

[0188] 27 Grealish, S. *et al.* Human ESC-derived dopamine neurons show similar preclinical efficacy and potency to fetal neurons when grafted in a rat model of Parkinson's disease. *Cell stem cell* **15**, 653-665 (2014).

[0189] 28 Kriks, S. *et al.* Dopamine neurons derived from human ES cells efficiently engraft in animal models of Parkinson's disease. *Nature* **480**, 547-551 (2011).

[0190] 29 Rodell, C. B., Dusaj, N. N., Highley, C. B. & Burdick, J. A. Injectable and cytocompatible tough double-network hydrogels through tandem supramolecular and covalent crosslinking. *Advanced materials* **28**, 8419-8424 (2016).

[0191] 30 Regmi, S., Fu, A. & Luo, K. Q. High shear stresses under exercise condition destroy circulating tumor cells in a microfluidic system. *Scientific reports* **7**, 39975 (2017).

[0192] 31 Leverett, L., Hellums, J., Alfrey, C. P. & Lynch, E. C. Red blood cell damage by shear stress. *Biophysical journal* **12**, 257-273 (1972).

[0193] 32 Food, U. & Administration, D. Guidance for FDA reviewers and sponsors: Content and review of chemistry, manufacturing, and control (CMC) information for human

somatic cell therapy investigational new drug applications (INDs). *Center for Biologics Evaluation and Research* (2008).

[0194] 33 Rehfeldt, F., Engler, A. J., Eckhardt, A., Ahmed, F. & Discher, D. E. Cell responses to the mechanochemical microenvironment—implications for regenerative medicine and drug delivery. *Advanced drug delivery reviews* **59**, 1329-1339 (2007).

[0195] 34 Rosales, A. M., Vega, S. L., DelRio, F. W., Burdick, J. A. & Anseth, K. S. Hydrogels with reversible mechanics to probe dynamic cell microenvironments. *Angewandte Chemie International Edition* **56**, 12132-12136 (2017).

[0196] 35 Vernon, B., Kim, S. W. & Bae, Y. H. Insulin release from islets of Langerhans entrapped in a poly (N-isopropylacrylamide-co-acrylic acid) polymer gel. *Journal of Biomaterials Science, Polymer Edition* **10**, 183-198 (1999).

[0197] 36 Lee, M. S., Lill, M. & Makkar, R. R. Stem cell transplantation in myocardial infarction. *Reviews in cardiovascular medicine* **5**, 82-98 (2004).

[0198] 37 Barattin, R. & Voyer, N. Chemical modifications of atomic force microscopy tips. *Atomic Force Microscopy in Biomedical Research: Methods and Protocols*, 457-483 (2011).

[0199] 38 Kubrova, E. *et al.* Hypothermia and nutrient deprivation alter viability of human adipose-derived mesenchymal stem cells. *Gene* **722**, 144058 (2020).

CLAIMS

1. Systems, devices, compositions and methods configured for delivering microgel-encapsulated cells in injectable formulations, essentially as disclosed herein.

2. An injectable formulation system comprising cells embedded within pore space of microscopic hydrogel particles, wherein while ensconced in this packed bed of microgels, the cells are protected from the shear stresses and shear stress gradients, wherein the chemical composition of the particles can be engineered to promote longevity and generation of the appropriate cellular phenotypes, and wherein the system is optionally configured to provide temporal control over exposure to growth factors, cytokines, and pharmacologic agents.

3. An injectable formulation system as disclosed and configured to effect swapping the solvent surrounding the cell laden hydrogel therapy and subsequently protecting the embedded cells during delivery to facilitate functional integration post-transplantation.

4. A microgel-based delivery system substantially as described herein and configured to encapsulate cells to protect the cells from physical damage due to shear and extensional flows during the transplantation process.

5. A microgel-based delivery system substantially as described herein and configured to be mechanically tunable, e.g. to increase the rate of cell engraftment post-transplantation by providing scaffolding for cells to migrate and integrate into the host circuitry.

6. A microgel-based delivery system substantially as described herein and configured for practical application to cell transplantation.

7. A microgel-based delivery system substantially as described herein and configured to provide a stable three-dimensional niche at the delivery site.

8. A microgel-based delivery system substantially as described herein and configured to encapsulate cells in the pore space between microscopic hydrogel particles (microgels), and employing yield stress fluid properties of packs of microgels to protect the cells from mechanical stress during delivery and to facilitate integration to the native tissue, wherein during delivery, the packs of microgels undergo plug flow in which the pressure drop across the length

of the pipe is compensated (preferably solely) by frictional forces at the interface between the pipe wall and microgels, and wherein at the delivery site, the pack of microgels behave as an elastic solid across the range of physiological frequencies and provide a stable 3D culture paradigm to support engraftment.

9. A microgel-based delivery system substantially as described herein and configured to encapsulate cells in the pore space of the microgel, and confine the formulation to a fixed volume to facilitate perfusing liquid freeze/thaw or maintenance media, differentiation factors, and anti-inflammatory agents prior to delivery to the tissue, making the formulation ammenable to transport and storage.

10. A microgel-based delivery system substantially as described herein and configured for use as a vehicle for delivery of therapeutic cells into an animal host, preferably wherein it can be used to encapsulate and deliver differentiated human pluripotent stem cells in regenerative medicine applications, or used to deliver differentiated neural cell types for regenerative therapies targeting a central nervous system pathology.

11. A method of delivering microgel-encapsulated cells in injectable formulations essentially as described herein, the method comprising:

employing yield stress fluid properties of packs of microgels to protect the cells from mechanical stress during delivery and to facilitate integration to the native tissue,

wherein during delivery, the packs of microgels undergo plug flow in which the pressure drop across the length of the pipe is compensated solely by frictional forces at the interface between the pipe wall and microgels,

wherein at the delivery site, the pack of microgels behave as an elastic solid across the range of physiological frequencies and provide a stable 3D culture paradigm to support engraftment.

12. A method of delivering microgel-encapsulated cells in injectable formulations essentially as described herein, the method comprising embedding cells within the pore space of microscopic hydrogel particles, wherein while ensconced in this packed bed of microgels, the cells are protected from shear stresses and shear stress gradients.

13. A method of delivering microgel-encapsulated cells in injectable formulations essentially as described herein, the method comprising steps:

a) mix aqueous and organic phases to perform inverse emulsion Michael addition crosslinking of HA w/DTT to generate spherical hydrogels;
b) homogenize mixture with fine blades to generate droplets whose diameters closely match those of cells. Smaller droplets are required for delivery through a thin needle / cannula;
c) wash microgels of organic phase to rid of excess organic phase (e.g. kerosene) and surfactant;
d) swell microgels in desired growth media to provide nutrient reserve for cells;
e) pipette mix cells into microgels at a volume fraction <20% to ensure shear protection capabilities of microgels is not diluted by cells;
f) load mixture into custom syringe (see diagram) to provide storage and transport, and facilitate cryopreservation; and
g) inject into patient to provide cell therapy.

14. A system, device, composition or method herein, wherein the adamantane and cyclodextrin (AC) concentration is less than a critical AC concentration wherein the stress required to break AC bonds and drive flow during injection exceeds microgel yield stress.

15. A system, device, composition or method herein, comprising use of highly monodisperse spherical microgels.

16. A system, device, composition or method herein, comprising a microgel fabrication protocol to generate particle diameters on the same order of magnitude as cell diameters, ensuring that the largest objects are 10x smaller than the roughly 200 μm (27 – 30G) cannula diameter commonly used in delivery of cell therapies..

17. A microfluidic platform configured to formulate NSC droplets within packs of HA microgels (Fig. 20), wherein cells are matured in spheroids using agar wells, low adhesion dishes, or hanging drop methods and subsequently isolated and encapsulated in the microgels prior to transplantation.

18. An injectable formulation deliver device providing solvent exchange, configured to confine the injectable formulation to a fixed volume with porous filters on the inlet and exit (Fig. 21), wherein microgels and cells are contained within this volume due to being larger than the mesh of the filters, such that different solvents can be flushed through the pores of the formulation.

Fig. 1a granular injectable fabrication and assembly

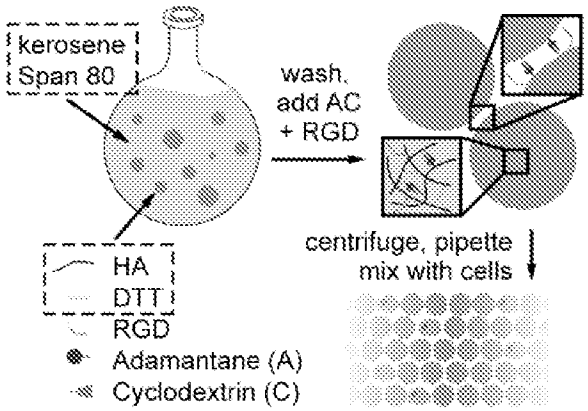


Fig. 1b granular flow shear protection

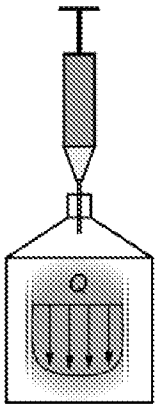


Fig. 1c injectable formulation testing platforms

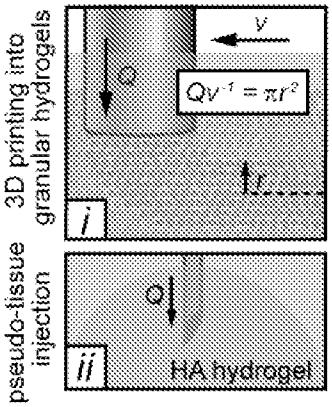


Fig. 2a

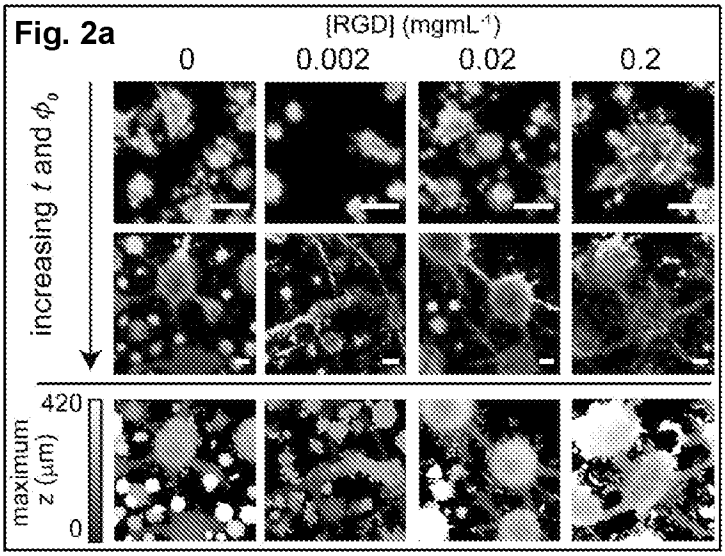


Fig. 2b

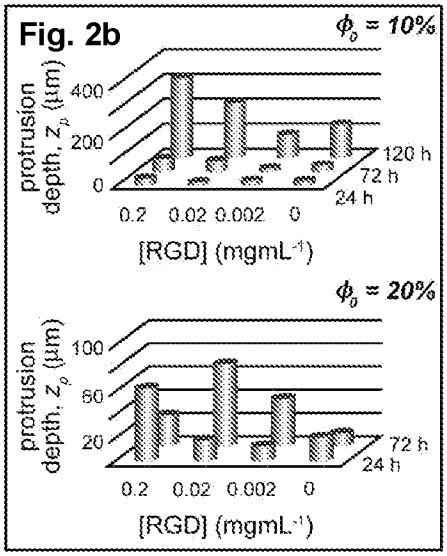


Fig. 3a

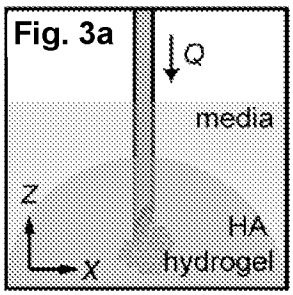


Fig. 3b

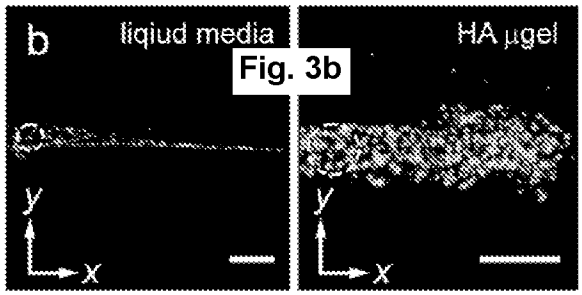


Fig. 3c

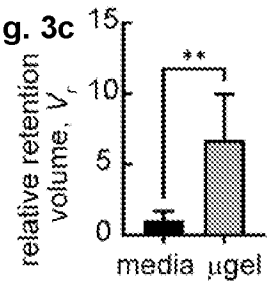


Fig. 4a

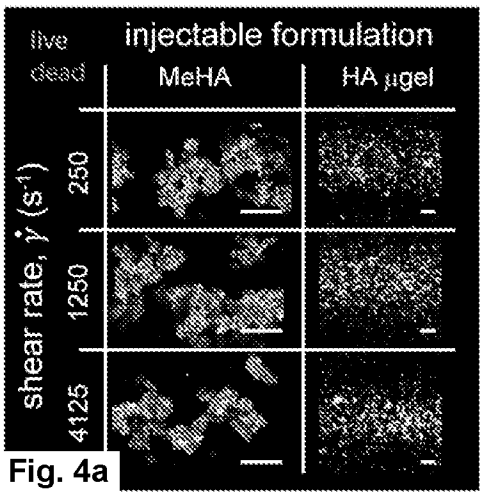


Fig. 4b shear rate, $\dot{\gamma}$ (s^{-1})

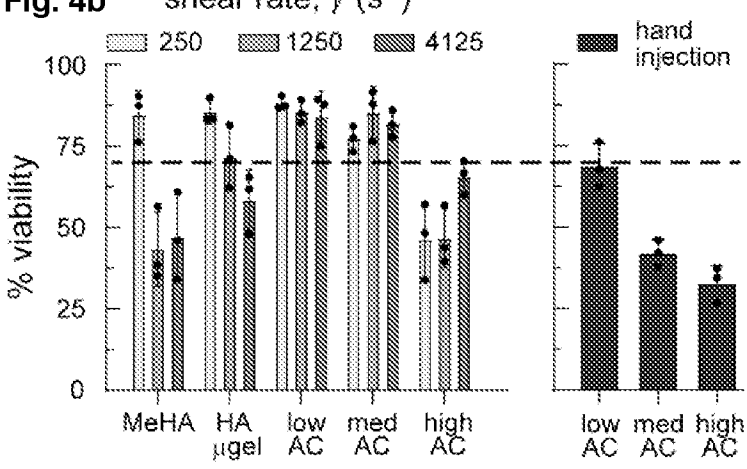


Fig. 5a

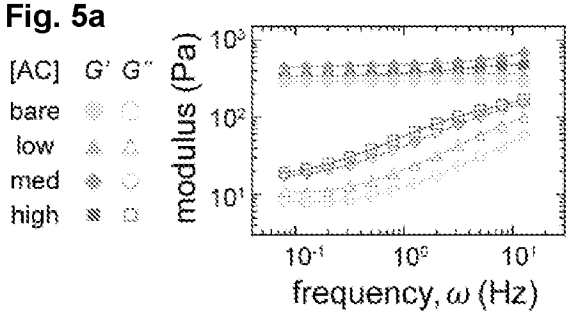


Fig. 5b

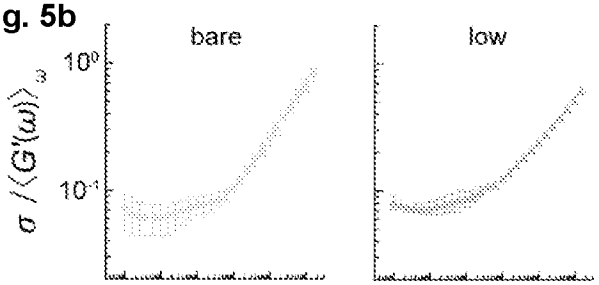


Fig. 5c

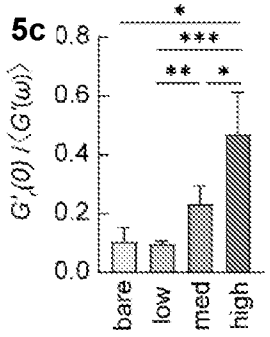
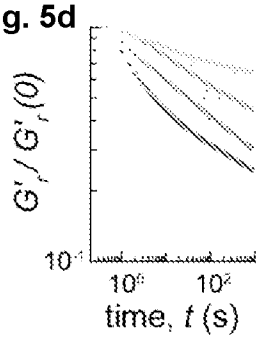
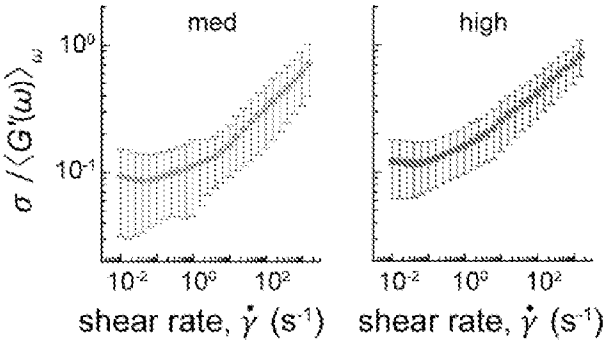


Fig. 5d





indentation analysis

Fig. 6a

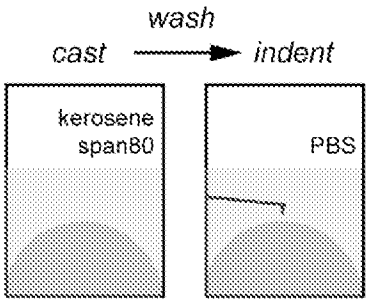


Fig. 6b

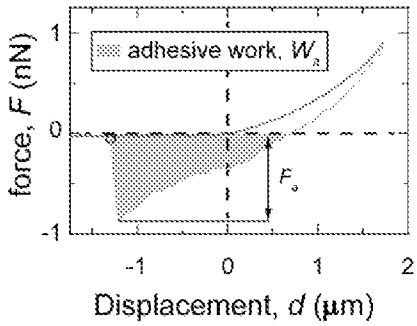
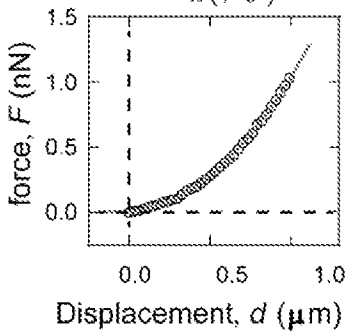


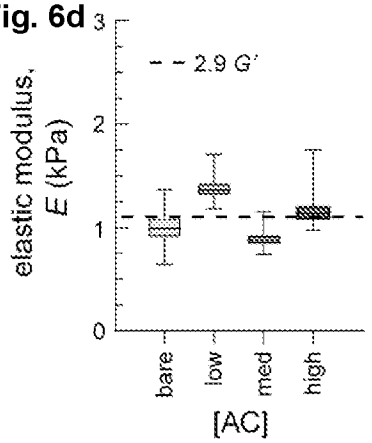
Fig. 6c

$$F = \frac{2E\tan(\alpha)d^2}{\pi(1-\upsilon^2)}$$



bare probe

Fig. 6d



adamantane probe

Fig. 6e

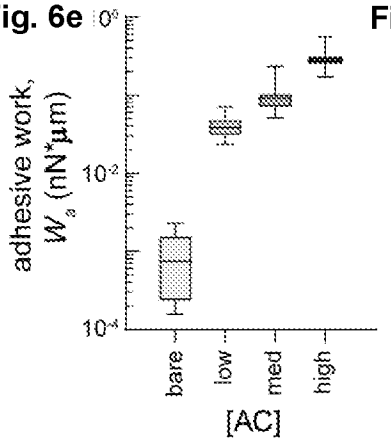


Fig. 6f

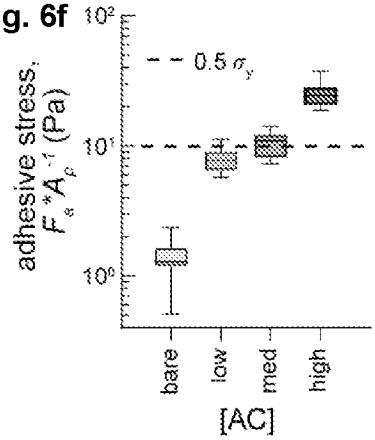


Fig. 7a

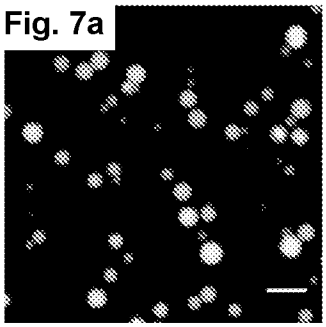


Fig. 7b

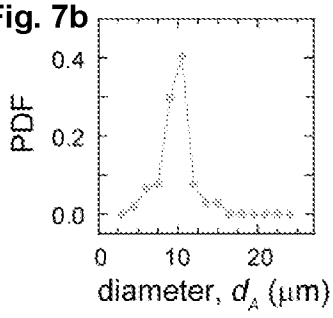


Fig. 8a

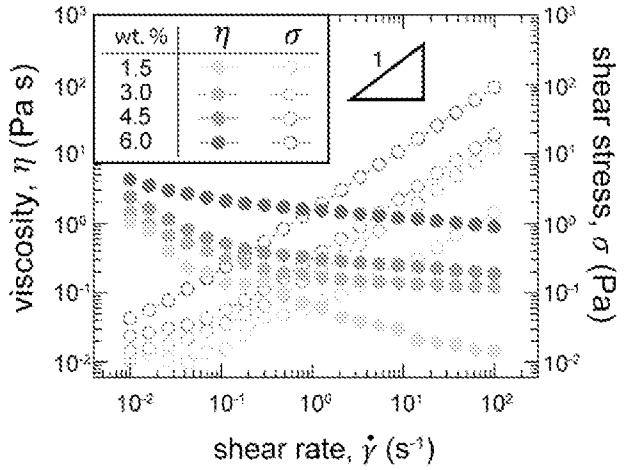


Fig. 8b

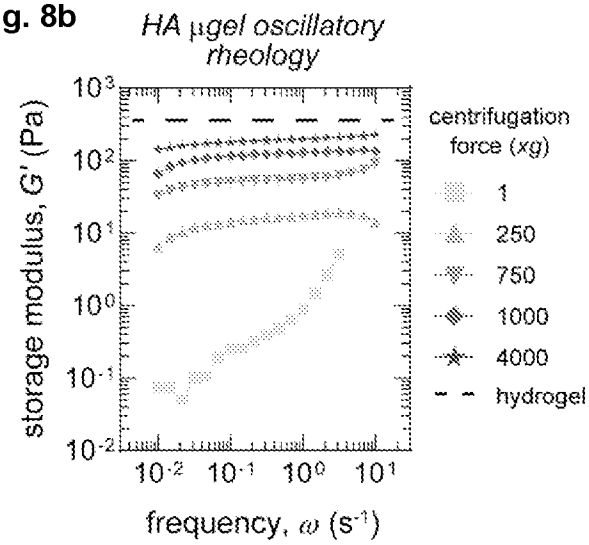
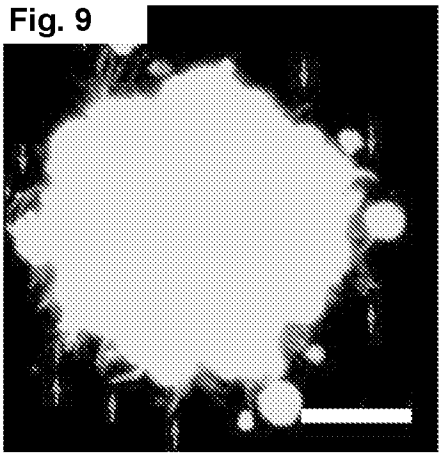


Fig. 9



[RGD] ($mgmL^{-1}$) Fig. 10

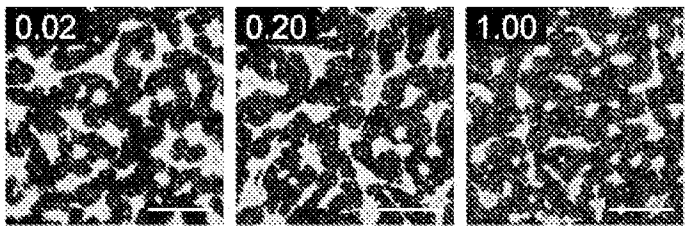


Fig. 11a

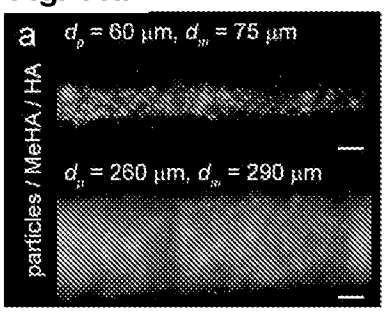


Fig. 11b

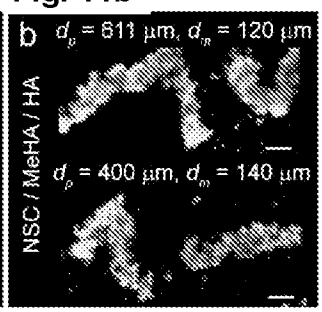


Fig. 11c

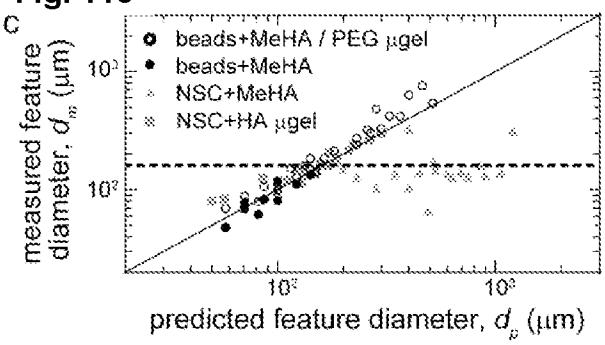


Fig. 12

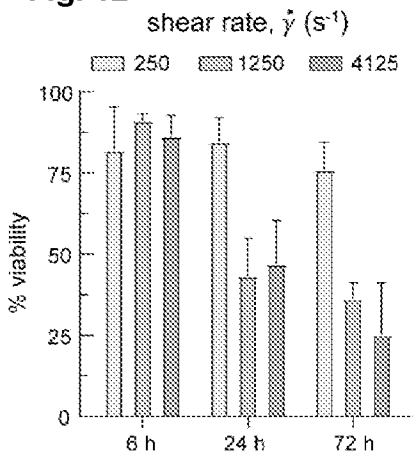


Fig. 15a

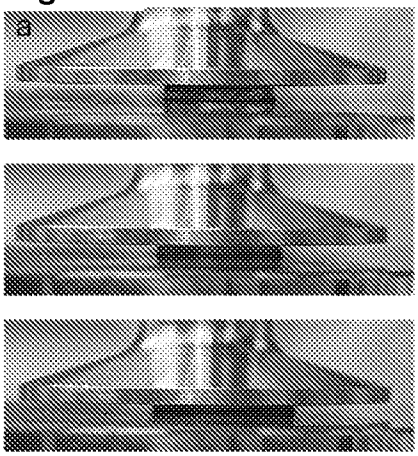


Fig. 15b

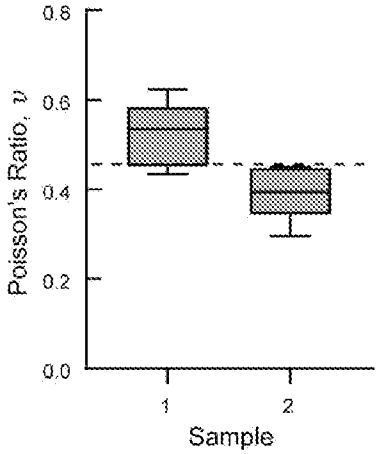


Fig. 13a

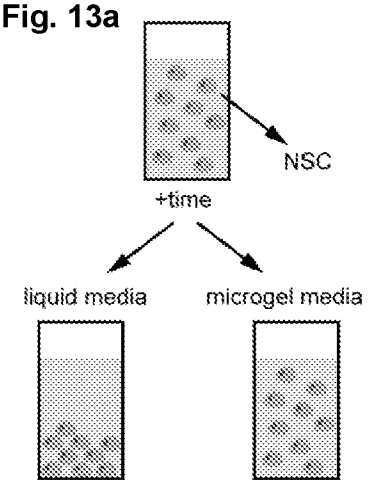


Fig. 13b

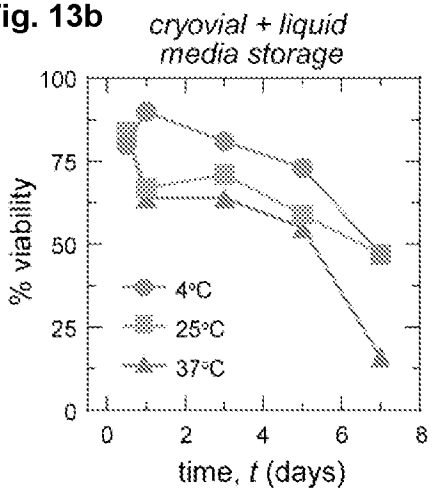


Fig. 13c

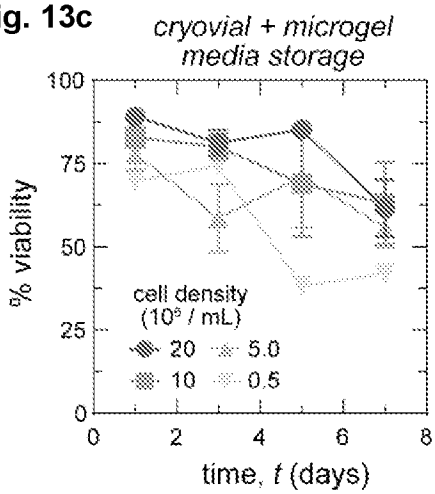


Fig. 14a

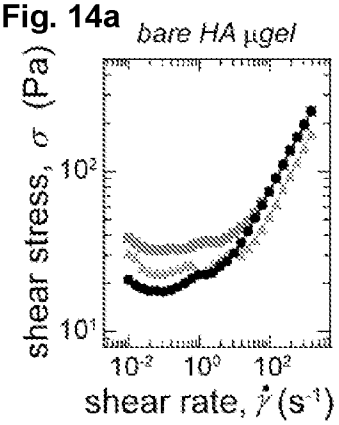


Fig. 14b

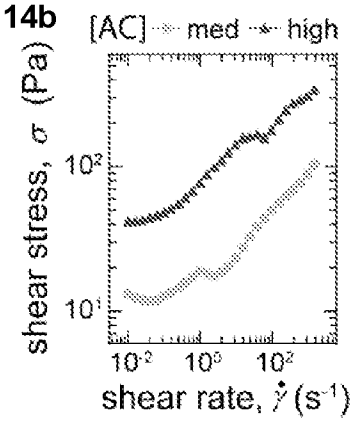


Fig. 14c

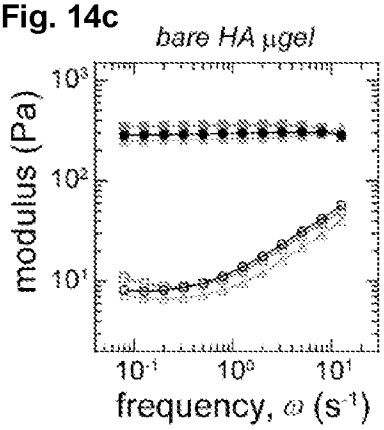


Fig. 16a *bare probe*

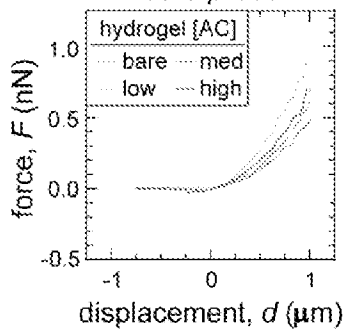


Fig. 16b *adamantane probe*

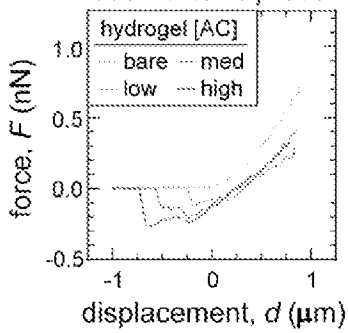


Fig. 16c

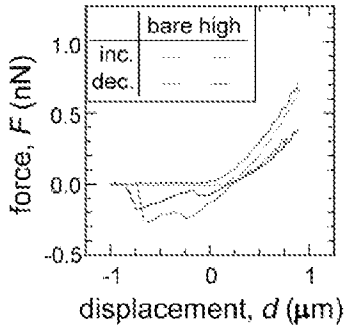


Fig. 17a

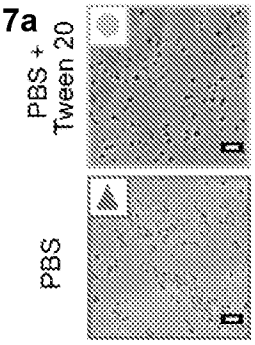


Fig. 17b

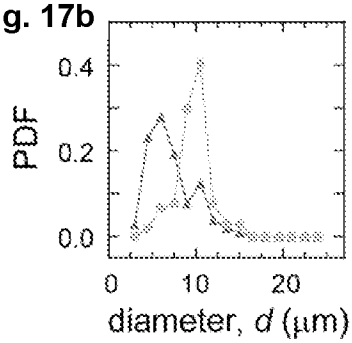


Fig. 17c

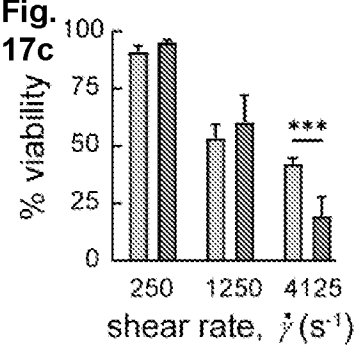


Fig. 17d

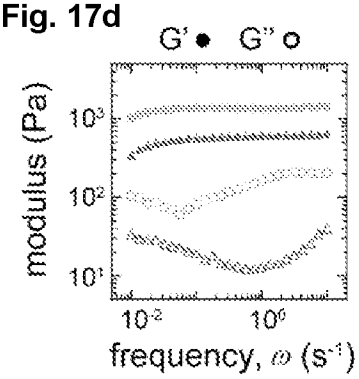


Fig. 17e

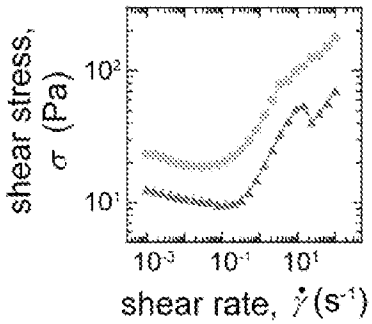


Fig. 17f

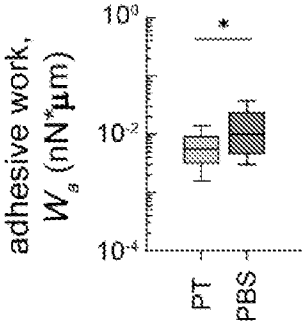


Fig. 18

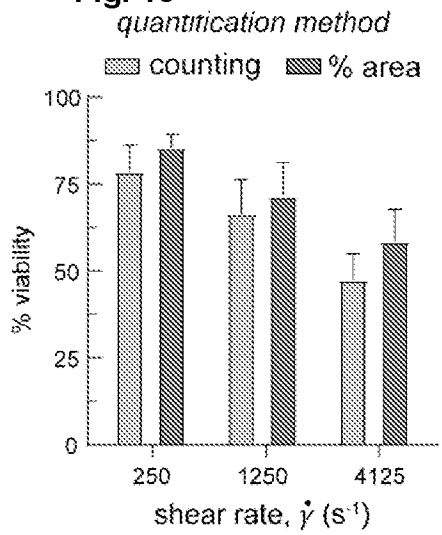


Fig. 19

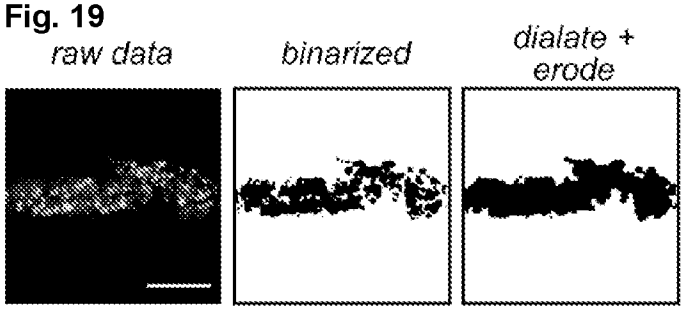


Fig. 20

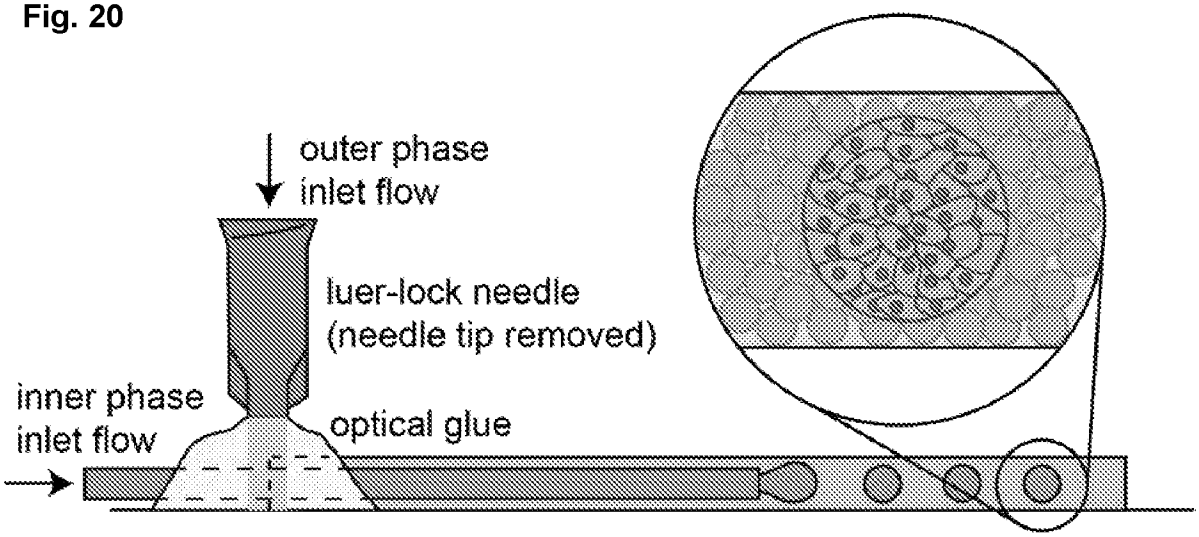
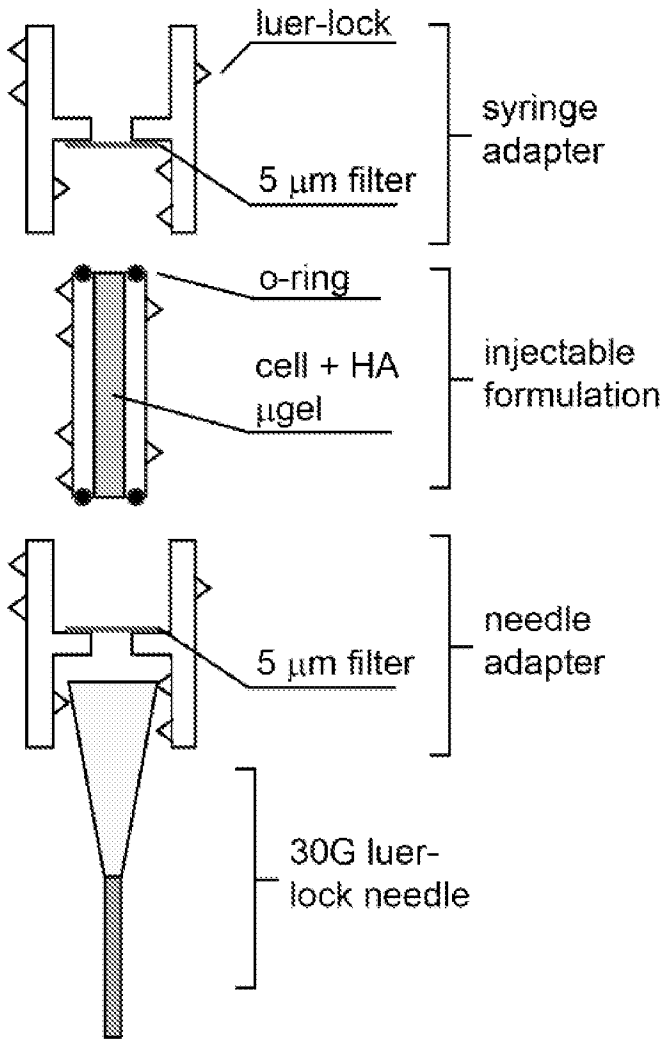

outer phase
inlet flow
luer-lock needle
(needle tip removed)
inner phase
inlet flow
optical glue

Fig. 21


luer-lock
5 μm filter
syringe
adapter
o-ring
cell + HA
μgel
injectable
formulation
5 μm filter
needle
adapter
30G luer-
lock needle

INTERNATIONAL SEARCH REPORT

International application No.
PCT/US 23/67267

A. CLASSIFICATION OF SUBJECT MATTER

IPC - INV. A61L 27/52, A61L 27/54 (2023.01)
ADD.

CPC - INV. A61L 27/52, A61L 27/54

ADD. A61L 2400/06, A61L 2430/00, Y10S 524/916

According to International Patent Classification (IPC) or to both national classification and IPC

B. FIELDS SEARCHED

Minimum documentation searched (classification system followed by classification symbols)
See Search History document

Documentation searched other than minimum documentation to the extent that such documents are included in the fields searched
See Search History document

Electronic data base consulted during the international search (name of data base and, where practicable, search terms used)
See Search History document

C. DOCUMENTS CONSIDERED TO BE RELEVANT

Category*	Citation of document, with indication, where appropriate, of the relevant passages	Relevant to claim No.
X	US 2020/0306413 A1 (The Regents of the University of California) 01 October 2020 (01.10.2020); entire document, but especially: para [0005], para [0018], para [0038], fig. 1A	2
L	Riley et al. "Granular Hydrogels: emergent properties of jammed hydrogel microparticles and their applications in tissue repair and regeneration" Current Opinion in Biotechnology, Vol 60 (December 2019): pages 1-8; entire document, but especially: page 7 para 3	2
X	US 2020/0254142 A1 (University of New Hampshire) 13 August 2020 (13.08.2020); entire document, but especially: para [0067], para [0070]	2
X, P	Qazi et al. "Anisotropic Rod-Shaped Particles Influence Injectable Granular Hydrogel Properties and Cell Invasion" Advanced Materials, Vol 34 Issue 12 (24 January 2022): pages 1-12; entire document, but especially: abstract, page 6 col 1 para 2, page 10 col 2 para 3, fig. 4a	2
X, P	Qazi et al. "Methods to Characterize Granular Hydrogel Rheological Properties, Porosity, and Cell Invasion" ACS Biomaterials Science & Engineering, Vol 8 Issue 4 (24 March 2022): entire document, but especially: page 1436 col 1 para 2- col 2 para 1, page 1437 col 2 para 4 to page 1438 col 1 para 2	2

☒ Further documents are listed in the continuation of Box C. ☐ See patent family annex.

* Special categories of cited documents:
"A" document defining the general state of the art which is not considered to be of particular relevance
"D" document cited by the applicant in the international application
"E" earlier application or patent but published on or after the international filing date
"L" document which may throw doubts on priority claim(s) or which is cited to establish the publication date of another citation or other special reason (as specified)
"O" document referring to an oral disclosure, use, exhibition or other means
"P" document published prior to the international filing date but later than the priority date claimed
"T" later document published after the international filing date or priority date and not in conflict with the application but cited to understand the principle or theory underlying the invention
"X" document of particular relevance; the claimed invention cannot be considered novel or cannot be considered to involve an inventive step when the document is taken alone
"Y" document of particular relevance; the claimed invention cannot be considered to involve an inventive step when the document is combined with one or more other such documents, such combination being obvious to a person skilled in the art
"&" document member of the same patent family

Date of the actual completion of the international search	Date of mailing of the international search report
31 August 2023	NOV 20 2023
Name and mailing address of the ISA/US Mail Stop PCT, Attn: ISA/US, Commissioner for Patents P.O. Box 1450, Alexandria, Virginia 22313-1450 Facsimile No. 571-273-8300	Authorized officer Kari Rodriquez Telephone No. PCT Helpdesk: 571-272-4300

INTERNATIONAL SEARCH REPORT

International application No.
PCT/US 23/67267

C (Continuation). DOCUMENTS CONSIDERED TO BE RELEVANT

Category*	Citation of document, with indication, where appropriate, of the relevant passages	Relevant to claim No.
A	US 2020/0085859 A1 (The Regents of the University of California) 19 March 2020 (19.03.2020); entire document	2
A, P	Feng et al. "Microgel assembly: Fabrication, characteristics and application in tissue engineering and regenerative medicine" Bioactive Materials, Vol 9 (17 July 2021): pages105-119; entire document	2
A, P	Ataie et al. "Nanoengineered Granular Hydrogel Bioinks with Preserved Interconnected Microporosity for Extrusion Bioprinting" nano micro small, Vol 18 Issue 37 (03 August 2022): pages 1-16; entire document, but especially: abstract, fig. 6a	2

INTERNATIONAL SEARCH REPORT

International application No.
PCT/US 23/67267

Box No. II Observations where certain claims were found unsearchable (Continuation of item 2 of first sheet)

This international search report has not been established in respect of certain claims under Article 17(2)(a) for the following reasons:

1. ☐ Claims Nos.:
because they relate to subject matter not required to be searched by this Authority, namely:

2. ☒ Claims Nos.: 1, 3-16
because they relate to parts of the international application that do not comply with the prescribed requirements to such an extent that no meaningful international search can be carried out, specifically:
Claims 1 and 3-16 are omnibus claims and are not drafted in accordance with Rule 6.2(a).

3. ☐ Claims Nos.:
because they are dependent claims and are not drafted in accordance with the second and third sentences of Rule 6.4(a).

Box No. III Observations where unity of invention is lacking (Continuation of item 3 of first sheet)

This International Searching Authority found multiple inventions in this international application, as follows:
---See Supplemental Sheet---

1. ☐ As all required additional search fees were timely paid by the applicant, this international search report covers all searchable claims.

2. ☐ As all searchable claims could be searched without effort justifying additional fees, this Authority did not invite payment of additional fees.

3. ☐ As only some of the required additional search fees were timely paid by the applicant, this international search report covers only those claims for which fees were paid, specifically claims Nos.:

4. ☒ No required additional search fees were timely paid by the applicant. Consequently, this international search report is restricted to the invention first mentioned in the claims; it is covered by claims Nos.:
2

Remark on Protest

☐ The additional search fees were accompanied by the applicant's protest and, where applicable, the payment of a protest fee.

☐ The additional search fees were accompanied by the applicant's protest but the applicable protest fee was not paid within the time limit specified in the invitation.

☐ No protest accompanied the payment of additional search fees.

INTERNATIONAL SEARCH REPORT
Information on patent family members

International application No.
PCT/US 23/67267

Lack of Unity Invention

This application contains the following inventions or groups of inventions which are not so linked as to form a single general inventive concept under PCT Rule 13.1. In order for all inventions to be searched, the appropriate additional search fees must be paid.

Group I: Claim 2 is directed to an injectable formulation system.

Group II: Claim 17 is directed to a microfluidic platform.

Group III: Claim 18 is directed to an injectable formulation deliver device providing solvent exchange.

The inventions listed as Groups I-III do not relate to a single general inventive concept under PCT Rule 13.1 because, under PCT Rule 13.2, they lack the same or corresponding special technical features for the following reasons:

SPECIAL TECHNICAL FEATURES

The invention of Group I includes the special technical feature of an injectable formulation system comprising cells embedded within pore space of microscopic hydrogel particles, not required by the claims of Groups II or III.

The invention of Group II includes the special technical feature of a microfluidic platform configured to formulate neural stem cells droplets within hyaluronic acid microgels, not required by the claims of Groups I or III.

The invention of Group III includes the special technical feature of an injectable formulation deliver device providing solvent exchange comprising an inlet comprising a first porous filter and an exit comprising a second porous filter, not required by the claims of Groups I or II.

COMMON TECHNICAL FEATURES

Groups I-IIII share the common technical feature of a formulation comprising microgels and cells. However, this shared technical feature does not represent a contribution over prior art as being anticipated by US 2020/0306413 A1 to The Regents of the University of California (hereinafter UC), which discloses of a formulation comprising microgels and cells (para [0005]: "In one embodiment, a hydrogel-based material... that is formed using annealed microgel particles..."; para [0038]: "Living cells that have anti-inflammatory potential... exist between microgel particles 12 in the interstitial spaces 14. When the microgel particles 12 are annealed, the cells are incorporated into the interstitial spaces 14..."; see fig. 1C and fig. 1D).

Groups I and III share the common technical feature of an injectable formulation comprising microgels and cells. However, this shared technical feature does not represent a contribution over prior art as being anticipated by UC, which discloses of an injectable formulation comprising microgels and cells (para [0005]: "In one embodiment, a hydrogel-based material... that is formed using annealed microgel particles... to generate synthetic, injectable therapies..."; para [0038]: "Living cells that have anti-inflammatory potential... exist between microgel particles 12 in the interstitial spaces 14. When the microgel particles 12 are annealed, the cells are incorporated into the interstitial spaces 14..."; see fig. 1C and fig. 1D).

As the common technical features were known in the art at the time of the invention, these cannot be considered special technical features that would otherwise unify the groups.

Therefore, Groups I-III lack unity under PCT Rule 13 because they do not share a same or corresponding special technical feature.

Item 4 (cont'd): Claims 1 and 13-16 are omnibus claims and are not drafted in accordance with Rule 6.2(a).

Notes to Application:

Claim 2 is unclear and confusing. The first claim element specifies that cells are "embedded" within microscopic hydrogel particles. However, the second claim element further recites "wherein while ensconced in this packed bed of microgels, the cells are protected." Thus, "packed bed of microgels" lacks antecedent basis, as does the term "ensconced." In the interest of completing the international search, the term "ensconced" has been interpreted to reference "embedded" and "packed bed of microgels" has been interpreted to reference the "microscopic hydrogel particles" (see also instant specification [004]).

Claims 17 and 18 both contain references to figures (Fig. 20 and Fig. 21, respectively). Because claim 17 and claim 18 can be interpreted without reference to Fig. 20 and Fig 21, references to those figures have been ignored.